# Controlling tunneling in ammonia isotopomers

Csaba Fábri, Roberto Marquardt, Attila G. Császár, and Martin Quack

Citation: J. Chem. Phys. **150**, 014102 (2019); doi: 10.1063/1.5063470
View online: https://doi.org/10.1063/1.5063470
View Table of Contents: http://aip.scitation.org/toc/jcp/150/1
Published by the American Institute of Physics

The Journal of Chemical Physics ARTICLE scitation.org/journal/jcp

# Controlling tunneling in ammonia isotopomers

Cite as: J. Chem. Phys. 150, 014102 (2019); doi: 10.1063/1.5063470
Submitted: 27 September 2018 • Accepted: 26 November 2018 •
Published Online: 3 January 2019



Csaba Fábri,[1,2,3,a)] Roberto Marquardt,[3,4] Attila G. Császár,[1,2] and Martin Quack[3,b)]

## AFFILIATIONS

[1] Laboratory of Molecular Structure and Dynamics, Institute of Chemistry, Eötvös Loránd University, Pázmány Péter sétány 1/A, H-1117 Budapest, Hungary
[2] MTA-ELTE Complex Chemical Systems Research Group, P.O. Box 32, H-1518 Budapest 112, Hungary
[3] Physical Chemistry, ETH Zürich, CH-8093 Zürich, Switzerland
[4] Laboratoire de Chimie Quantique, Institut de Chimie UMR 7177 CNRS/Université de Strasbourg, 4, Rue Blaise Pascal CS 90032, 67081 Strasbourg Cedex, France

[a)] **Electronic mail:** ficsaba@caesar.elte.hu
[b)] **Electronic mail:** quack@ir.phys.chem.ethz.ch

## ABSTRACT

We report results of full-dimensional variational rovibrational quantum-dynamical computations for several ammonia isotopomers, based on selected potential energy and electric dipole moment hypersurfaces. The variational rovibrational eigenstates have been used as a basis for the solution of the time-dependent Schrödinger equation for nuclear motion including coherent infrared multiphoton excitation. The theoretical and computational framework developed during this study enables the investigation of the coherent inhibition or enhancement of tunneling in ammonia isotopomers by appropriately chosen laser fields. Our quantum-dynamical computations include all vibrational and rotational degrees of freedom and assume neither the alignment nor the orientation of the molecules under investigation. Specific results include accurate rotational-vibrational levels for $NH_2D$, $NHD_2$, NHDMu, and NHDT, probability densities for structural parameters as a function of time from the full-dimensional wavepacket results, time-dependent chirality for the isotopically chiral molecule NHDT, and detailed analyses of the enhancement and inhibition of stereomutation dynamics.



## I. INTRODUCTION

Since the early days of quantum mechanics, ammonia and its isotopomers have been prototypical molecules for molecular spectroscopy and quantum-mechanical tunneling dynamics.[1–3] While early treatments of the nuclear motions of ammonia were usually restricted to one-dimensional descriptions, extended models including several degrees of freedom and full-dimensional potential energy hypersurfaces (PES) have become available for the vibrational-tunneling motion of polyatomic molecules (see Refs. 4–17 and references cited therein), upon which extended dynamical treatments could be based. In particular, for $NH_3$, extended line lists[16–18] have been computed variationally, utilizing, among others, the TROVE program package.[19–21] Furthermore, the promotion and inhibition of tunneling via different nuclear degrees of freedom[22–27] have been investigated and a general algorithm was presented to take into account the quadrupole-hyperfine effects in $NH_3$[28] (see also Ref. 29 for recent experiments).

A comparison of results from stationary-state high-resolution spectroscopy with variationally computed rovibrational eigenstates has demonstrated the considerable progress achieved in the formulation of accurate PES and the solution of the time-independent nuclear motion Schrödinger equation (see Refs. 4–12, 30, and 31 and references cited therein). Much less work is available on the explicitly time-dependent quantum dynamics of either isolated molecules or molecules under the influence of a coherent radiation field. The present work represents a move in this direction and it pays particular attention to the chiral ammonia isotopomer NHDT (see Fig. 1). The time-dependent study of NHDT allows us to gain insight into a prototypical stereomutation reaction converting enantiomers by inversion, to be compared to a

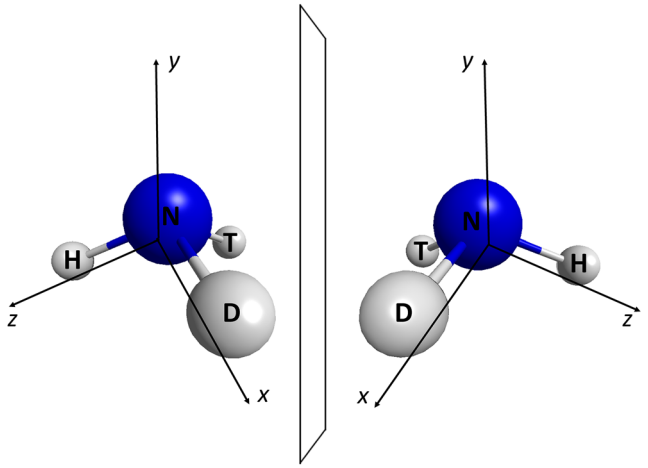


**FIG. 1**. Structures of the two enantiomers of NHDT. The orientation of the coordinate axes on the left-hand side corresponds to the definition of the axes used in this study.

related stereomutation by internal rotation in molecules such as hydrogen peroxide, HOOH.[10–12]

In treating time-dependent quantum-mechanical molecular motion numerically, one can follow two basic approaches: (a) solve the time-dependent Schrödinger equation (TDSE) or an equivalent time-dependent differential equation directly by an appropriate algorithm, which is typically iterative;[32–40] (b) solve the time-dependent problem in two steps. First, solve the time-independent Schrödinger equation (TISE) and obtain molecular eigenstates which are spectroscopic states; the results can be compared with high-resolution energy levels and transition moments. In the second step, one then derives from Schrödinger's separation ansatz[41] the time-dependent wave function ("wavepacket") and other time-dependent molecular quantities, either for the isolated molecule or for the system interacting with a coherent radiation field.[42–47]

The advantage of the first approach is its relative simplicity, as it does not require the calculation of eigenstates, which becomes difficult with increasing dimensionality. The first approach is particularly suitable for short-time dynamics. As we have pointed out in relation to the theory of coherent infrared multiphoton excitation, the second approach has several distinct advantages.[42–48] At the end of the first step of the two-step approach, one can compare the computed results with those derived from high-resolution spectroscopy, frequently available with very high accuracy, and thus test some of the underlying approximations, such as the PES used. This advantage is particularly pronounced because of the recent development of efficient computer codes for rovibrational eigenstate computations.[4–12,30,31] Furthermore, in the second step, involving the time evolution, one can design suitable approximations, such as the quasiresonant approximation (QRA) or the Floquet–Lyapunov approximation for coherent excitation,[42–44] which facilitate long-time propagation, not easily accessible to direct approaches. Last but not least, within the second approach, it is very easy to vary the initial condition of the dynamical calculation with almost no additional computational effort. In the present work, we have chosen to pursue the second approach, which one might call "divide and rule" (in Latin "divide et impera," DEI), because the division of the computational process into two stages results in better control (or "ruling") in both the separate first and second stages.

The significance of quantum-mechanical tunneling can hardly be overstated.[49] Tunneling, a fundamentally important and intrinsically quantum-mechanical effect, is discussed in every elementary textbook on quantum mechanics and has been found to play an important role in chemical processes ranging from enzyme catalysis[50] to relatively simple rearrangements of atoms in molecules.[51,52] Tunneling has been evoked as the key mechanism in low temperature diffusion of adsorbates,[53] even for particles as heavy as the CO molecule.[54] The problem of driven tunneling, i.e., tunneling through a barrier in the presence of time-dependent external fields, is of considerable practical importance in various scientific disciplines, e.g., in the control of chemical reactions by laser pulses,[55–64] in solid state,[65,66] ultracold,[67] and attosecond physics,[68] where driven tunneling is vital for understanding the mechanism of high harmonic generation.[69–71] Recently, the control of tunneling switching in *m*-D-phenol has led to the demonstration of a molecular quantum switch.[72]

In what follows, we describe the accurate computational investigation of the quantum dynamics of tunneling in a symmetric double-well potential in realistic molecular systems using multidimensional models. This endeavor required the extension of the fourth-age[4] quantum-chemical variational nuclear-motion code GENIUSH[73–76] with time-dependent quantum-dynamical features. The extended version of GENIUSH is applied to investigate the quantum dynamics of selected $NH_3$ isotopomers, with particular emphasis on the coherent inhibition and enhancement of tunneling by laser fields (see also previous studies on the time-dependent quantum dynamics of $NH_3$ isotopomers[77–87]). Our time-dependent quantum-dynamical computations, unlike the previous ones, treat all vibrational and rotational degrees of freedom in a numerically exact fashion.

The structure of the paper is as follows. In Sec. II, the time-independent and time-dependent theoretical developments, including the technical aspects of our computations, are outlined. In Sec. III, we describe the time-independent results (rovibrational energy eigenstates) obtained for $NH_3$ and the other selected isotopomers. These time-independent results are utilized in Sec. IV, where we summarize the time-dependent results for the coherent inhibition and enhancement of tunneling by appropriately designed nonresonant laser fields. The nuclear motion flux[88–97] in relation to tunneling is also addressed in Sec. IV. Section V summarizes the most important results of this study. Some preliminary results related to the present work were reported at conferences (see Refs. 85–87).

## II. THEORY

### A. General approach

The molecular wave function for nuclear motion within the Born–Oppenheimer[98,99] or a more general electronically adiabatic approximation, disregarding dynamical effects from nuclear spin (except symmetry effects), can be obtained from the TDSE ($i = \sqrt{-1}$)

$$i\frac{h}{2\pi}\frac{\partial\Psi(x_1,y_1,z_1,\ldots,x_{3N},y_{3N},z_{3N},t)}{\partial t} = \hat{H}(t)\Psi(x_1,y_1,z_1,\ldots,x_{3N},y_{3N},z_{3N},t), \quad (1)$$

where $x_k$, $y_k$, $z_k$ are the Cartesian nuclear coordinates of an N-atomic molecule and $h$ is the Planck constant. The general solution for the wave function $\Psi(x_1, y_1, z_1, \ldots, x_{3N}, y_{3N}, z_{3N}, t)$ with a time-dependent Hamiltonian $\hat{H}(t)$ can be obtained by means of the $\hat{U}(t, t_0)$ time-evolution operator

$$\Psi(x_1,y_1,z_1,\ldots,x_{3N},y_{3N},z_{3N},t) = \hat{U}(t,t_0)\Psi(x_1,y_1,z_1,\ldots,x_{3N},y_{3N},z_{3N},t_0). \quad (2)$$

The time-evolution operator satisfies the equation

$$i\frac{h}{2\pi}\frac{d\hat{U}(t,t_0)}{dt} = \hat{H}(t)\hat{U}(t,t_0) \quad (3)$$

with the initial condition $\hat{U}(t_0, t_0) = \hat{1}$, where $\hat{1}$ denotes the identity operator. $\hat{U}(t, t_0)$ provides also the explicit time-dependent solution of the Liouville–von Neumann equation

$$i\frac{h}{2\pi}\frac{d\hat{\varrho}(t)}{dt} = [\hat{H}(t),\hat{\varrho}(t)] \quad (4)$$

for the density operator

$$\hat{\varrho}(t) = \sum_k p_k(t)|\psi_k\rangle\langle\psi_k| \quad (5)$$

with

$$\hat{\varrho}(t) = \hat{U}(t,t_0)\hat{\varrho}(t_0)\hat{U}^\dagger(t,t_0). \quad (6)$$

In Eq. (5), $|\psi_k\rangle$ is usually an eigenstate of the isolated molecule. $\hat{U}(t, t_0)$ also describes the time dependence of any observable $\hat{Q}$ described by the Heisenberg equation of motion

$$\hat{Q}(t) = \hat{U}^\dagger(t,t_0)\hat{Q}(t_0)\hat{U}(t,t_0). \quad (7)$$

Thus, once $\hat{U}(t, t_0)$ is obtained, one can derive any desired time-dependent quantity. In particular, for the time-dependent probability density in coordinate space, one has

$$P(x_1,y_1,z_1,\ldots,x_{3N},y_{3N},z_{3N},t) = |\Psi(x_1,y_1,z_1,\ldots,x_{3N},y_{3N},z_{3N},t)|^2, \quad (8)$$

which is often called a wavepacket and describes the quantum dynamics of the time-dependent molecular structure. A description of the flux density associated with nuclear motion and its relation to the probability density will be provided in Sec. II G. In practice, we obtain a numerical solution of the TDSE and the Liouville–von Neumann equation by means of a matrix representation of the relevant quantities in the basis of molecular eigenstates of the isolated molecule, as described in detail in Secs. II B–II H (see also Ref. 3 for the general background).

### B. Solution of the nuclear-motion Schrödinger equation

The rotational-vibrational Hamiltonian of an N-atomic molecule (with $D \le 3N - 6$ active vibrational degrees of freedom, including possibly large-amplitude motions, internal rotation, and the three rotational degrees of freedom, while the center-of-mass motion is separated) expressed in general internal coordinates has the form

$$\hat{H} = \hat{T}_v + \hat{T}_r + \hat{T}_{rv} + \hat{V} = \hat{H}_v + \hat{T}_r + \hat{T}_{rv}, \quad (9)$$

where

$$\hat{H}_v = \hat{T}_v + \hat{V} = \frac{1}{2}\sum_{k=1}^{D}\sum_{l=1}^{D}\tilde{g}^{-1/4}\hat{p}_k^\dagger G_{kl}\tilde{g}^{1/2}\hat{p}_l\tilde{g}^{-1/4} + \hat{V}, \quad (10)$$

$$\hat{T}_r = \frac{1}{2}\sum_{\alpha=1}^{3}G_{\alpha+D,\alpha+D}\hat{J}_\alpha^2 + \frac{1}{2}\sum_{\alpha=1}^{3}\sum_{\beta=\alpha+1}^{3}G_{\alpha+D,\beta+D}[\hat{J}_\alpha,\hat{J}_\beta]_+, \quad (11)$$

and

$$\hat{T}_{rv} = \frac{1}{2}\sum_{\alpha=1}^{3}\sum_{k=1}^{D}(\hat{p}_k^\dagger G_{k,\alpha+D} + G_{k,\alpha+D}\hat{p}_k)\hat{J}_\alpha. \quad (12)$$

The different quantities present in the vibrational ($\hat{T}_v$) and rotational ($\hat{T}_r$) kinetic energy operators as well as in the rotational-vibrational coupling (Coriolis) term ($\hat{T}_{rv}$) are defined as follows (see also Refs. 73 and 74):

$$\begin{aligned} g_{kl} &= \sum_{i=1}^{N} m_i\frac{\partial\mathbf{x}_i^T}{\partial q_k}\frac{\partial\mathbf{x}_i}{\partial q_l}, \\ g_{k,\alpha+D} &= \sum_{i=1}^{N} m_i\frac{\partial\mathbf{x}_i^T}{\partial q_k}(\mathbf{e}_\alpha\times\mathbf{x}_i), \\ g_{\alpha+D,\beta+D} &= \sum_{i=1}^{N} m_i(\mathbf{e}_\alpha\times\mathbf{x}_i)^T(\mathbf{e}_\beta\times\mathbf{x}_i), \end{aligned} \quad (13)$$

where $m_i$ and $\mathbf{x}_i$ denote the masses (see also Sec. II H) and the body-fixed (BF) position vectors of the nuclei, $\mathbf{e}_\alpha$ is a unit vector along the $\alpha$th axis of the body-fixed frame, $\mathbf{G} = \mathbf{g}^{-1}$, and $\tilde{g} = \det(\mathbf{g})$. Solution of the vibrational Schrödinger equation

$$\hat{H}_v\Phi_i = E_i\Phi_i \quad (14)$$

results in vibrational energy levels $E_i$ and vibrational eigenstates $\Phi_i$. In order to solve the vibrational (tunneling) Schrödinger equation, an appropriate set of vibrational basis functions must be found. The version of GENIUSH extended for this study employs contractions of vibrational basis functions that have been applied successfully for the solution of the vibrational Schrödinger equation in previous work.[30,100] In the particular case of $NH_3$-like systems, the six-dimensional (6D) vibrational problem can be naturally split into 3D bending and 3D stretching problems (with coordinates $\mathbf{q}_b$ and $\mathbf{q}_s$,

respectively). The contracted vibrational basis is constructed as a direct product of 3D bending and 3D stretching eigenfunctions $b(\mathbf{q}_b)$ and $s(\mathbf{q}_s)$, which are further expanded in terms of direct-product discrete variable representation (DVR) basis functions[31,101]

$$b(\mathbf{q}_b) = \sum_{i=1}^{N_b} b_i \phi_i(\mathbf{q}_b),$$
$$s(\mathbf{q}_s) = \sum_{j=1}^{N_s} s_j \phi_j(\mathbf{q}_s), \tag{15}$$

where $\phi_i(\mathbf{q}_b)$ and $\phi_j(\mathbf{q}_s)$ denote the bending and stretching direct-product DVR functions. In order to represent the vibrational eigenstates, we employ contracted vibrational basis functions

$$\Phi_i(\mathbf{q}_b, \mathbf{q}_s) = \sum_b \sum_s c_{bs}^i b(\mathbf{q}_b) s(\mathbf{q}_s). \tag{16}$$

The vibrational Hamiltonian matrix is set up by evaluating matrix elements of $\hat{H}_v$ in the contracted vibrational basis.

The calculation of the potential energy matrix elements requires the evaluation of multidimensional integrals. For the specific case of contracted vibrational functions, these integrals can be efficiently evaluated by applying the technique of sequential summation.[102] After inserting the definitions of $b(\mathbf{q}_b)$ and $s(\mathbf{q}_s)$, given in Eq. (15),

$$\left\langle bs|\hat{V}|b's'\right\rangle = \sum_{i=1}^{N_b} b_i b_i' \sum_{j=1}^{N_s} s_j s_j' V(\mathbf{q}_{b,i}, \mathbf{q}_{s,j}), \tag{17}$$

where $V(\mathbf{q}_{b,i}, \mathbf{q}_{s,j})$ is the value of $\hat{V}$ at the 6D grid point $(\mathbf{q}_{b,i}, \mathbf{q}_{s,j})$. The basic idea of sequential summation is obvious from Eq. (17), the sum over $j$ is evaluated first and the result is stored for each $\mathbf{q}_{b,i}$ grid point (or vice versa), beating the unfavorable scaling of the brute force double summation over $i$ and $j$. The same idea can be utilized for the evaluation of the vibrational kinetic energy matrix elements

$$\left\langle bs\left|\hat{T}_v\right|b's'\right\rangle = \frac{1}{2}\sum_{k=1}^{D}\sum_{l=1}^{D}\left\langle bs\left|\tilde{g}^{-1/4}\hat{p}_k^\dagger G_{kl}\tilde{g}^{1/2}\hat{p}_l\tilde{g}^{-1/4}\right|b's'\right\rangle$$
$$= \frac{1}{2}\sum_{k=1}^{D}\sum_{l=1}^{D}\left\langle(\tilde{g}_b^{-1/4}b)(\tilde{g}_s^{-1/4}s)\right|$$
$$\hat{p}_k^\dagger G_{kl}\tilde{g}^{1/2}\hat{p}_l\left|(\tilde{g}_b^{-1/4}b')(\tilde{g}_s^{-1/4}s')\right\rangle. \tag{18}$$

In Eq. (18), we assume that $\tilde{g} = \det(\mathbf{g})$, also related to the integration volume element, can be factorized as

$$\tilde{g}(\mathbf{q}_b, \mathbf{q}_s) = \tilde{g}_b(\mathbf{q}_b)\tilde{g}_s(\mathbf{q}_s). \tag{19}$$

Therefore, $\tilde{g}_b^{-1/4}$ and $\tilde{g}_s^{-1/4}$ can be absorbed into $b$ ($b'$) and $s$ ($s'$), meaning that matrix elements of the operators $\hat{p}_k^\dagger G_{kl}\tilde{g}^{1/2}\hat{p}_l$ have to be evaluated in the basis $(\tilde{g}_b^{-1/4}b)(\tilde{g}_s^{-1/4}s)$. The evaluation is done by inserting two resolutions of the identity in between $\hat{p}_k^\dagger$ and $G_{kl}\tilde{g}^{1/2}$, as well as $G_{kl}\tilde{g}^{1/2}$ and $\hat{p}_l$. As $G_{kl}\tilde{g}^{1/2}$ depends only on the vibrational coordinates, one can employ sequential summation to evaluate the $G_{kl}\tilde{g}^{1/2}$ matrix elements in the contracted basis. Finally, matrix elements of $\hat{p}_k$ can be obtained from well-known formulae in the DVR, as these operators are proportional to the first-derivative operator with respect to a single vibrational coordinate. The factorization condition of Eq. (19) holds for all coordinate systems used in this study, including Radau coordinates.[103]

The resulting vibrational Hamiltonian matrix must be diagonalized to obtain $E_i$ and $\Phi_i$. First, we note that contracted basis functions automatically form a symmetry-adapted vibrational basis, i.e., they transform according to irreducible representations of the appropriate molecular symmetry (MS) group.[104] This helps diagonalizing separately the noninteracting blocks of $\mathbf{H}_v$ corresponding to different irreducible representations. Moreover, it is plausible that basis functions $|bs\rangle$ with high bending and stretching energy eigenvalues (denoted by $E_b$ and $E_s$) are less important; thus, we introduce the criterion

$$E_b + E_s < E_{\text{threshold}}, \tag{20}$$

where $E_{\text{threshold}}$ is an appropriately chosen energy threshold. Vibrational basis functions not satisfying Eq. (20) are discarded.

After obtaining the solution of the vibrational problem, one can move to the computation of energy levels and eigenstates with nonzero rotational angular momentum quantum number $J$ ($J > 0$). The vibrational subspace (VS) method[76,105] used by GENIUSH has been adapted to work with the contracted vibrational basis. The VS wave-function ansatz reads as

$$\psi = \sum_{i=1}^{n}\sum_{j=1}^{2J+1} c_{ij}\Phi_i R_j, \tag{21}$$

where the vibrational eigenstates $\Phi_i$ are combined with $2J + 1$ $R_j$ rotational basis functions (either symmetric-top eigenfunctions or rigid-rotor eigenfunctions[106] corresponding to an appropriately selected geometry of the molecule). In order to set up the matrix representation of the rovibrational Hamiltonian, the matrix elements

$$\left\langle\Phi_i R_j\left|\hat{H}\right|\Phi_k R_l\right\rangle = E_i\delta_{ik}\delta_{jl} + \left\langle\Phi_i R_j\left|\hat{T}_r + \hat{T}_{rv}\right|\Phi_k R_l\right\rangle \tag{22}$$

have to be evaluated. It is obvious that Eq. (22) requires the computation of the matrix elements of the operators $G_{\alpha+D,\beta+D}$ and $G_{k,\alpha+D}\hat{p}_k$ in the contracted vibrational basis. This can be achieved by the procedure outlined in Eqs. (17) and (18).

It is crucial to obtain a good separation of vibrational and rotational degrees of freedom if the aim is to apply the VS wave function ansatz defined in Eq. (21). GENIUSH is able to employ the Eckart frame[107] for arbitrary vibrational coordinates with either fixed or flexible reference structures.[75,108] The present implementation uses the recently published quaternion-based Eckart transformation algorithm of Ref. 109. For the notations used here for molecular symmetry, see Refs. 29 and 110 and references cited therein.

### C. Assignment of numerically exact eigenstates with approximate ("good") quantum numbers for zeroth-order states

Although the current implementation of GENIUSH provides the exact rotational quantum number, $J$, and irreducible representations, $\Gamma$, of the MS group for the eigenstates, approximate "good" quantum numbers assignable to appropriate underlying zeroth-order states do not follow automatically from the computations. Thus, we implemented a hierarchical approach, outlined below for the special case of $NH_3$ isotopomers (the approach can be readily generalized to other systems).

First, the dominant $b(\mathbf{q}_b)s(\mathbf{q}_s)$ basis state giving the largest $|c^i_{bs}|$ value is selected for each vibrational eigenstate. Next, bending and stretching basis functions [$b(\mathbf{q}_b)$ and $s(\mathbf{q}_s)$, respectively] are examined separately. In the case of the stretching functions, each $s(\mathbf{q}_s)$ is decomposed as a linear combination of 3D harmonic-oscillator eigenfunctions and assigned with the harmonic-oscillator quantum numbers of the dominant harmonic-oscillator basis states. The $b(\mathbf{q}_b)$ 3D bending functions are expanded in terms of the product of 2D angular bending and 1D inversion functions, obtained as solutions of a 2D angular bending (keeping the inversion and all stretching coordinates fixed) and a 1D inversion (keeping all stretching and angular bending coordinates fixed) Schrödinger equation. The reduced-dimensional Schrödinger equation was defined by fixing the inactive coordinates at their equilibrium values and deleting the rows and columns corresponding to the inactive coordinates from the $\mathbf{g}$ matrix [see Eq. (13)] in all cases. The 2D angular bending and 1D inversion basis states can be assigned with approximate vibrational quantum numbers in a straightforward manner by either evaluating their overlaps with harmonic-oscillator eigenfunctions (2D angular bending case) or inspecting the corresponding energy level and parity values (1D inversion case). Similar overlap-based strategies have been employed for the assignment of rovibrational states.[111–113] Finally, we note that this approach obviously breaks down for eigenstates that are strong mixtures of the basis states. In this study, we selected a threshold of 0.8 on a scale of 1.0 for the absolute value of dominant overlaps to decide whether an eigenstate can be uniquely assigned with approximate "good" quantum numbers or not.

### D. Solution of the TDSE under the influence of a classical coherent radiation field

The TDSE for the specific case of a molecule under the influence of a coherent classical radiation field has the form

$$\mathrm{i}\frac{h}{2\pi}\frac{\partial\Psi(\mathbf{Q},t)}{\partial t} = (\hat{H}_0 + \hat{W}(t))\Psi(\mathbf{Q},t), \tag{23}$$

where $\hat{H}_0$ is the Hamiltonian of the isolated molecule described by a general set of coordinates $\mathbf{Q}$, and the explicitly time-dependent interaction term $\hat{W}(t)$ is given within the electric dipole approximation by

$$\hat{W}(t) = -\boldsymbol{\mu}_{\mathrm{el}}\mathbf{E}(t), \tag{24}$$

where $\boldsymbol{\mu}_{\mathrm{el}}$ is the electric dipole moment operator and $\mathbf{E}(t)$ is a time-dependent external electric field.[3] One way of solving the TDSE is to represent the time-dependent wave function $\Psi(\mathbf{Q}, t)$ as a linear combination of the rovibrational eigenstates

$$\Psi(\mathbf{Q},t) = \sum_{k=1}^{N} b_k(t)\psi_k(\mathbf{Q}). \tag{25}$$

This ansatz yields a set of coupled first-order differential equations

$$\mathrm{i}\frac{h}{2\pi}\dot{b}_j(t) = E_j b_j(t) + \sum_{k=1}^{N} W_{jk}(t)b_k(t), \quad j = 1,\ldots,N, \tag{26}$$

where $W_{jk}(t) = \langle\psi_j(\mathbf{Q})|\hat{W}(t)|\psi_k(\mathbf{Q})\rangle$ is a matrix element of $\hat{W}(t)$ in the eigenstate basis and $E_j$ is the energy level associated with the eigenstate $\psi_j(\mathbf{Q})$. It is advantageous to transform Eq. (26) first to the interaction picture. In the case of a nearly monochromatic (laser) radiation with $\mathbf{E}(t) = \mathbf{E}_0\cos(\omega t)$, it is additionally interesting to represent the problem in the quasiresonant basis[42] by means of the relation (set the zero-point energy level to $E_0 = 0$)

$$\omega_j = n_j\omega + x_j, \tag{27}$$

where $\omega_j = 2\pi E_j/h$, $\omega$ is the laser carrier angular frequency, and $n_j$ is an integer value defined in such a way that the corresponding resonance defect, $x_j$, satisfies $|x_j| < \omega/2$. The state vector $\mathbf{b}(t)$ must be transformed accordingly and in the quasiresonant basis we get

$$a_j(t) = \mathrm{e}^{\mathrm{i}(\omega_j - x_j)t}b_j(t) = \mathrm{e}^{\mathrm{i}n_j\omega t}b_j(t). \tag{28}$$

If $\hat{W}(t) = \hat{V}f(t)\cos(\omega t + \eta)$, the resulting set of equations takes the form

$$\mathrm{i}\dot{a}_j(t) = x_j a_j(t) + \frac{\pi}{h}\sum_{k=1}^{N} V_{jk}\left(\mathrm{e}^{\mathrm{i}(n_j - n_k + 1)\omega t} + \mathrm{e}^{\mathrm{i}(n_j - n_k - 1)\omega t}\right)a_k(t), \tag{29}$$

where the phase is set to zero ($\eta = 0$) and $f(t) \equiv 1$ is assumed for the sake of simplicity.

In this study, Eq. (29) is solved numerically, without introducing the quasi-resonant approximation (QRA). The solution strategy employs time discretization with an appropriately fine time step [for which $\hat{W}(t)$ can be regarded as constant] and applies the Chebyshev expansion method[34,35] to evaluate matrix exponentials. The use of QRA may become necessary when calculating evolution under long-time excitation and one can then use the more accurate Floquet[114] approximation (see Refs. 42, 46, and 115 for various alternatives). The QRA provides physical insight in terms of its time-independent effective Hamiltonian, very similar to the dressed-atom picture.[116–118]

As the interpretation of our time-dependent quantum-dynamical results relies on the Floquet formalism[114] (sometimes called Floquet–Lyapunov formalism[42]), a brief review of

the necessary theory is provided here. If the time-dependent Hamiltonian $\hat{H}(t) = \hat{H}(t + T)$ is periodic with a time period $T$, as in the case of the molecular interaction with a strictly monochromatic radiation, the Floquet theorem[114] assures that the solutions of the TDSE can be written as

$$\Psi(t) = \Theta(t)\exp(-i2\pi\epsilon t/h), \tag{30}$$

where $\Theta(t) = \Theta(t + T)$ is a periodic function with a time period $T$, with $\Theta(0) = \Psi(0)$, and $\epsilon$ is the quasienergy corresponding to the Floquet state $\Theta(t)$. Substituting the wave function ansatz of Eq. (30) into the TDSE yields the eigenvalue equation

$$\hat{H}_F\Theta_k(t) = \left(\hat{H}(t) - i\frac{h}{2\pi}\frac{\partial}{\partial t}\right)\Theta_k(t) = \epsilon_k\Theta_k(t), \tag{31}$$

where $\hat{H}_F$ is the Floquet Hamiltonian. The eigenvalue equation of Eq. (31) is usually transformed to a time-independent system of linear equations by the Fourier expansion of the periodic Floquet states $\Theta_k(t)$.[119] The general solution of the TDSE can be expressed as the superposition of Floquet states

$$\Psi(t) = \sum_k c_k \exp(-i2\pi\epsilon_k t/h)\Theta_k(t), \tag{32}$$

where $c_k = \langle\Theta_k(0)|\Psi(0)\rangle$ is a time-independent coefficient. The field-free time evolution is

$$\Psi(t) = \sum_k a_k \exp(-i2\pi E_k t/h)\psi_k, \tag{33}$$

where $a_k = \langle\psi_k|\Psi(0)\rangle$, which is analogous with the time evolution in Eq. (32), where a periodic excitation is assumed, and the Floquet states $\Theta_k(t)$ and the quasienergies $\epsilon_k$ play the role of the eigenstates $\psi_k$ and energy levels $E_k$, respectively. The Floquet Hamiltonian, due to the symmetry properties of the field-free Hamiltonian and the electric dipole moment operator, and due to the periodic time dependence of the interaction Hamiltonian, is invariant under the generalized parity operation $\mathbf{x}_i \to -\mathbf{x}_i$ and $t \to t + T/2$.[120] Therefore, the Floquet states can be classified into states of even and odd generalized parities, and only quasienergies of different generalized parities are allowed to cross if the laser parameters are varied.

### E. Interaction matrix elements

We consider the interaction of the molecule with a $z$-polarized time-dependent periodic electric field and supplement the field-free molecular Hamiltonian $\hat{H}_0$ with a classical electric dipole interaction term $\hat{W}(t)$ yielding

$$\hat{H}(t) = \hat{H}_0 + \hat{W}(t) = \hat{H}_0 - \hat{\mu}_z^{SF}E_0 f(t)\cos(\omega t + \eta), \tag{34}$$

where $\hat{\mu}_z^{SF}$ is the space-fixed $z$ component of $\boldsymbol{\mu}_{el}$, while $E_0$, $\omega$, and $\eta$ denote the amplitude, the carrier angular frequency, and the phase of the time-dependent electric field, respectively. Furthermore, $f(t)$ is a time-dependent envelope function, the time variation $df/dt$ of which is supposed to be much smaller than $\omega$. The interaction term of the Hamiltonian in Eq. (34) gives rise to the matrix elements

$$\left\langle\psi'\middle|\hat{\mu}_z^{SF}\middle|\psi\right\rangle = \sum_{i=1}^{n}\sum_{j=1}^{2J'+1}\sum_{k=1}^{n}\sum_{l=1}^{2J+1} c'_{ij}c_{kl}\sum_{\alpha=-1}^{1}\left\langle\Phi_i\middle|\hat{\mu}_\alpha^{BF}\middle|\Phi_k\right\rangle\left\langle R_j\middle|D_{0\alpha}^{1*}\middle|R_l\right\rangle, \tag{35}$$

where the rovibrational eigenstates $\psi'$ and $\psi$ are expanded according to the vibrational subspace ansatz [see Eq. (21)], $\hat{\mu}_z^{SF}$ is expressed in terms of spherical vector operator components $\hat{\mu}_\alpha^{BF}$ (with $\alpha = +1, 0, -1$), and BF refers to the body-fixed frame. As $\hat{\mu}^{BF}$ is expressed in the spherical basis, its rotation from the space-fixed frame to the body-fixed frame is described by the Wigner D matrix elements $D_{0\alpha}^{1*}$.[106,121] Evaluation of $\left\langle\Phi_i\middle|\hat{\mu}_\alpha^{BF}\middle|\Phi_k\right\rangle$ requires the considerations presented in Eqs. (17) and (18). To compute the matrix elements $\left\langle R_j\middle|D_{0\alpha}^{1*}\middle|R_l\right\rangle$, we expand $|R_j\rangle$ in terms of symmetric-top eigenfunctions $|JKM\rangle$,

$$|R_j\rangle = \sum_{K=-J}^{J} a_{jK}|JKM\rangle, \tag{36}$$

and then evaluate the resulting matrix elements

$$\langle J'K'M'\middle|D_{0\alpha}^{1*}\middle|JKM\rangle = (-1)^{M'-K'}\sqrt{(2J'+1)(2J+1)} \times \begin{pmatrix} J' & 1 & J \\ -M' & 0 & M \end{pmatrix}\begin{pmatrix} J' & 1 & J \\ -K' & \alpha & K \end{pmatrix} \tag{37}$$

analytically.[106,121] The 3$j$ symbols in Eq. (37) give rise to the following selection rules: $|J' - J| = 1$ (if $J = 0$ or $J' = 0$) or $|J' - J| = 0, 1$ (otherwise), and $M' = M$.

### F. Coherent inhibition and enhancement of tunneling in double-well systems

The general considerations presented up to this point are useful when one aims at inhibiting or enhancing tunneling in a symmetric double-well potential. Tunneling in a symmetric double-well system leads to the splitting of energy levels, and the eigenstates are either symmetric or antisymmetric with respect to inversion. Even though the eigenstates are delocalized, it is straightforward to construct nonstationary quantum states localized in one of the equivalent potential wells. One simple example for such localized quantum states is the

$$\Psi(t = 0) = \frac{1}{\sqrt{2}}(\Phi_{v^+} + \Phi_{v^-}) \tag{38}$$

superposition of the symmetric $\Phi_{v^+}$ and antisymmetric $\Phi_{v^-}$ eigenstates of a given tunneling doublet. The field-free time evolution of the initial state in Eq. (38) is described by the equation

$$\Psi(t) = \frac{1}{\sqrt{2}}\exp(-i2\pi E_{v^+}t/h)\Phi_{v^+} + \frac{1}{\sqrt{2}}\exp(-i2\pi E_{v^-}t/h)\Phi_{v^-}, \tag{39}$$

giving rise to a periodic time evolution of the revival probability $p_{rev}(t) = |\langle\Psi(0)|\Psi(t)\rangle|^2 = \cos^2(\pi\Delta E_{\pm,v}t/h)$ with a period

$\tau_v = h/|\Delta E_{\pm,v}|$, where $\Delta E_{\pm,v} = E_{v^-} - E_{v^+}$ denotes the tunneling splitting. At $t = \tau_v/2$, the quantum state, disregarding the absolute phase, becomes $(\Phi_{v^+} - \Phi_{v^-})/\sqrt{2}$, corresponding to a quantum state localized in the "other" potential well. In what follows, we describe two different laser-excitation schemes that are able to either keep the quantum state of Eq. (38) localized or shorten the field-free tunneling time $\tau_v/2$, leading to a faster conversion from $(\Phi_{v^+} + \Phi_{v^-})/\sqrt{2}$ to $(\Phi_{v^+} - \Phi_{v^-})/\sqrt{2}$.

As to the coherent inhibition of tunneling, we have adapted the strategy of Ref. 122, called coherent destruction of tunneling (CDT) there. If the molecule interacts with a continuous-wave monochromatic laser, the general solution of the TDSE takes the form

$$\Psi(t) = \sum_{k=1}^{2} c_k \exp(-i2\pi\epsilon_k t/h)\Theta_k(t), \tag{40}$$

where we have assumed that $\Psi(t)$ can be represented as a superposition of two Floquet states. If parameters of the laser (such as its frequency and intensity) are chosen in such a way that the two quasienergies in Eq. (40) are equal, $\epsilon_1 = \epsilon_2 = \epsilon$, i.e.,

$$\Psi(t) = \exp(-i2\pi\epsilon t/h)\sum_{k=1}^{2} c_k\Theta_k(t), \tag{41}$$

the relative phase between $\Theta_1(t)$ and $\Theta_2(t)$ in Eq. (41) does not change over time, and only a time-dependent absolute phase is acquired by the initially localized quantum state. Qualitatively speaking, tunneling is completely suppressed (or at least slowed down substantially) if $\epsilon_1 \approx \epsilon_2$, and the initially localized wavepacket remains localized due to the periodic external driving force. Another method for the suppression of tunneling was reported in Ref. 123.

Besides the coherent inhibition of tunneling, it is also of interest to devise schemes that increase the tunneling rate. A method able to enhance tunneling was reported in Ref. 124, and it relies on the application of the adiabatic Floquet theory[125] and a laser pulse with a smooth envelope function. In the adiabatic regime of suitably long laser pulses, the time evolution of $\Psi(t)$ can be expressed as

$$\Psi(t) = \sum_{k=1}^{2} c_k \exp\left(-i\frac{2\pi}{h}\int_0^t \epsilon_k(t')dt'\right)\Theta_k(t), \tag{42}$$

where $\epsilon_k(t)$ and $\Theta_k(t)$ are the quasienergies and Floquet states corresponding to the instantaneous laser intensity. Under the influence of a smooth laser pulse of length $t_p$, due to the adiabatic principle, $\Phi_{v^+}$ and $\Phi_{v^-}$ evolve into $\Theta_1(t)$ and $\Theta_2(t)$ and then return to $\Phi_{v^+}$ and $\Phi_{v^-}$ at the end of the laser pulse; thus, the quantum state at $t_p$ becomes

$$\Psi(t_p) = \frac{1}{\sqrt{2}}\exp\left(-i\frac{2\pi}{h}\int_0^{t_p}\epsilon_1(t)dt\right)\Phi_{v^+} + \frac{1}{\sqrt{2}}\exp\left(-i\frac{2\pi}{h}\int_0^{t_p}\epsilon_2(t)dt\right)\Phi_{v^-}, \tag{43}$$

meaning that a relative phase of $2\pi/h\int_0^{t_p}(\epsilon_2(t) - \epsilon_1(t))dt$ is acquired. The desired conversion from $(\Phi_{v^+} + \Phi_{v^-})/\sqrt{2}$ to $(\Phi_{v^+} - \Phi_{v^-})/\sqrt{2}$ (aside from an absolute phase) implies that

$$\int_0^{t_p}(\epsilon_2(t) - \epsilon_1(t))dt = \frac{h}{2}. \tag{44}$$

Provided that $\epsilon_2(t) - \epsilon_1(t) \geq \Delta E_{\pm,v}$ over the course of the laser pulse, the actual tunneling time $t_p$ will be shorter than its field-free counterpart $\tau_v/2$, leading to coherent enhancement of tunneling. Another method for the enhancement of tunneling was described in Ref. 126.

### G. Evaluation of the flux associated with nuclear motion

In addition to the time evolution of the probability density $P(\mathbf{Q}, t)$, one can also investigate the flux related to nuclear motions. This was already done in the early days of quantum mechanics.[127] Later, the concept of flux proved to be important in the evaluation of reaction rate coefficients.[128–133] Theoretical[88–96] and experimental investigations describing the reconstruction of the nuclear flux density from high-resolution pump-probe measurements[97] have been published by Manz and co-workers,[88–97] leading to the observation of interesting quantum effects. Fluxes have also been discussed in the statistical master equation description of unimolecular reactions.[134]

In this section, we review the elements of nuclear flux theory[92] relevant for this study. The link between $P(\mathbf{Q},t)$ and the current density $\mathbf{j}(\mathbf{Q}, t)$ is expressed by the continuity equation

$$\frac{\partial P}{\partial t} + \mathrm{div}\mathbf{j} = 0. \tag{45}$$

By employing Gauss's theorem, we get

$$\iiint_V \mathrm{div}\mathbf{j}\,dV = -\frac{\partial}{\partial t}\iiint_V P\,dV = \oiint \mathbf{j}\,d\mathbf{A} = F \tag{46}$$

for the flux F, where V is a closed volume in the configurational space and the surface integral is evaluated over the closed surface of V (note that V is defined in such a way that bound-state probability densities are practically zero at its external boundaries). Next, we express the probability of finding the system in V

$$P_V = \iiint_V P\,dV = \iiint_V |\Psi|^2\,dV = \langle\Psi|\hat{h}|\Psi\rangle, \tag{47}$$

with $\hat{h}$ being a step function whose value is 1 inside the closed volume V and 0 otherwise [to be precise, we employ the so-called half-maximum convention, see also Eq. (51) for a special case]. As $P_V$ is obtained as the expectation value of $\hat{h}$, F can be expressed by means of the Ehrenfest theorem[116]

as

$$F = -\frac{\partial P_V}{\partial t}$$
$$= -\frac{2\pi i}{h}\left\langle \Psi \middle| [\hat{H}, \hat{h}] \middle| \Psi \right\rangle = -\frac{2\pi i}{h}\sum_{jk} c_j^*(t)c_k(t)\left\langle \psi_j \middle| [\hat{H}, \hat{h}] \middle| \psi_k \right\rangle$$
$$= -\frac{2\pi i}{h}\sum_{jk} c_j^*(0)c_k(0)\exp(i\omega_{jk}t)(E_j - E_k)\left\langle \psi_j \middle| \hat{h} \middle| \psi_k \right\rangle$$
$$= \frac{4\pi}{h}\sum_{j<k} \mathrm{Im}[c_j^*(0)c_k(0)\exp(i\omega_{jk}t)](E_j - E_k)\left\langle \psi_j \middle| \hat{h} \middle| \psi_k \right\rangle, \quad (48)$$

where $\psi_j$ and $E_j$ are the rovibrational eigenstates and eigenvalues, $\omega_{jk} = 2\pi(E_j - E_k)/h$, and real $\langle\psi_j|\hat{h}|\psi_k\rangle$ matrix elements and field-free conditions are assumed, i.e., $c_k(t) = c_k(0)\exp(-i2\pi E_k t/h)$. As the $\psi_j$ and $E_j$ quantities are provided by GENIUSH, Eq. (48) can be employed directly for the evaluation of F.

If the initial state

$$\Psi(t = 0) = \frac{1}{\sqrt{2}}(\Phi_{v^+} + \Phi_{v^-}) \quad (49)$$

is constructed as the symmetric linear combination of the symmetric and antisymmetric tunneling eigenstates $\Phi_{v^+}$ and $\Phi_{v^-}$ of a selected vibrational state for a symmetric double-well system, the general formula presented in Eq. (48) simplifies to

$$F = \frac{2\pi\Delta E_{\pm,v}}{h}\left\langle \Phi_{v^+} \middle| \hat{h} \middle| \Phi_{v^-} \right\rangle \sin\left(\frac{2\pi\Delta E_{\pm,v}}{h}t\right), \quad (50)$$

where $\Delta E_{\pm,v} = E_{v^-} - E_{v^+}$ denotes the tunneling splitting corresponding to the selected tunneling doublet. If we aim at describing the coherent tunneling process in $NH_3$, the step function $\hat{h}$ in Eq. (50) is defined as

$$\hat{h}(\mathbf{Q}; \theta_0) = \begin{cases} 1, & \text{if } \theta > \theta_0 \\ 0, & \text{if } \theta < \theta_0 \\ \frac{1}{2}, & \text{if } \theta = \theta_0 \end{cases}, \quad (51)$$

where $\theta$ is the inversion angle, ranging from 0° to 180° ($\theta_0 = 90°$ corresponds to the planar geometry), and the so-called half-maximum convention is applied for the definition of $\hat{h}$.

### H. Technical aspects and comparison with the quasiadiabatic-channel reaction-path Hamiltonian approximation

In order to construct the kinetic-energy operator, one has to specify a set of vibrational coordinates. Our computations employ the well-known orthogonal Radau coordinates;[103] the three Radau vectors can be parametrized with three distances ($r_1$, $r_2$, $r_3$), two polar angles ($\vartheta_1$, $\vartheta_2$), and one azimuthal angle ($\varphi$), where the latter, which is different from $\theta$ in Eq. (51), is an alternative coordinate to describe the inversion (see also Ref. 78). The 3D stretching and the 3D bending vibrational models needed to construct the 6D contracted vibrational basis were defined by fixing inactive vibrational coordinates at their equilibrium values. The resulting 3D stretching and 3D bending Schrödinger equations were solved in a direct-product DVR vibrational basis; for distances ($r_1$, $r_2$, $r_3$), polar angles ($\vartheta_1$, $\vartheta_2$), and azimuthal angles ($\varphi$), we utilized 1D DVR bases based on Laguerre polynomials, Legendre polynomials, and periodic complex exponential functions, respectively. Next, the 3D stretching and 3D bending eigenfunctions were combined to a 6D contracted vibrational basis. Atomic masses, $m_H$ = 1.007 825 u, $m_D$ = 2.014 102 u, $m_T$ = 3.016 049 u, $m_{Mu}$ = 0.113 977 u, and $m_N$ = 14.003 074 u, were used throughout the nuclear motion computations.

In this study, we employed the global AMMPOT4[14] and the refined NH3-Y2010[17] PES. In addition to the GENIUSH computations, we used the quasiadiabatic-channel reaction-path Hamiltonian (RPH) method[10,11,135,136] to obtain vibrational energy levels and tunneling splittings. In essence, the RPH approach uses a vibrationally adiabatic separation of the large-amplitude motion in a selected coordinate from the other degrees of freedom and is a physically insightful approximation of the full-dimensional treatment. We refer to the literature for background information[137–139] and for a detailed description of the methods used.[10,11,135,136] Two different electric dipole moment surfaces (DMS)[15,16] were considered to describe the interaction of the molecule with a time-dependent external electric field. The DMS of Ref. 15 was used for our time-dependent quantum-dynamical computations. The electric dipole moment matrix elements corresponding to the DMS of Ref. 15 are in good agreement with the data calculated using the DMS of Ref. 16.

## III. RESULTS FOR ROVIBRATIONAL ENERGY LEVELS AND EIGENSTATES

This section presents the comparison of the global AMMPOT4[14] (with modest refinement using experimental data) and the refined NH3-Y2010[17] PES. The AMMPOT4 vibrational energy levels are in excellent agreement with the results of Ref. 14. One way to characterize the global performance of these PES is to evaluate and compare the number of vibrational eigenstates W(E) up to a given vibrational energy E. Figure 2 gives the W(E) function for selected $NH_3$ isotopomers. It is apparent that the differences $\Delta W(E) = W(E)_{AMMPOT4} - W(E)_{NH3-Y2010}$ between the AMMPOT4 and NH3-Y2010 PES become more pronounced with increasing vibrational energy. Nevertheless, the differences remain moderate even for highly excited vibrational eigenstates and they tend to scatter around $\Delta W = 0$.

In addition to the variational (VAR) GENIUSH treatment outlined in Sec. II, we also employed the RPH method with the AMMPOT4 PES for $NH_2D$, $NHD_2$, and NHDT. Vibrational energy levels and tunneling splittings obtained by the VAR and RPH methods were compared to assess the performance of the RPH method. Numerical values of the vibrational energy levels and tunneling splittings are given in Tables I–III for

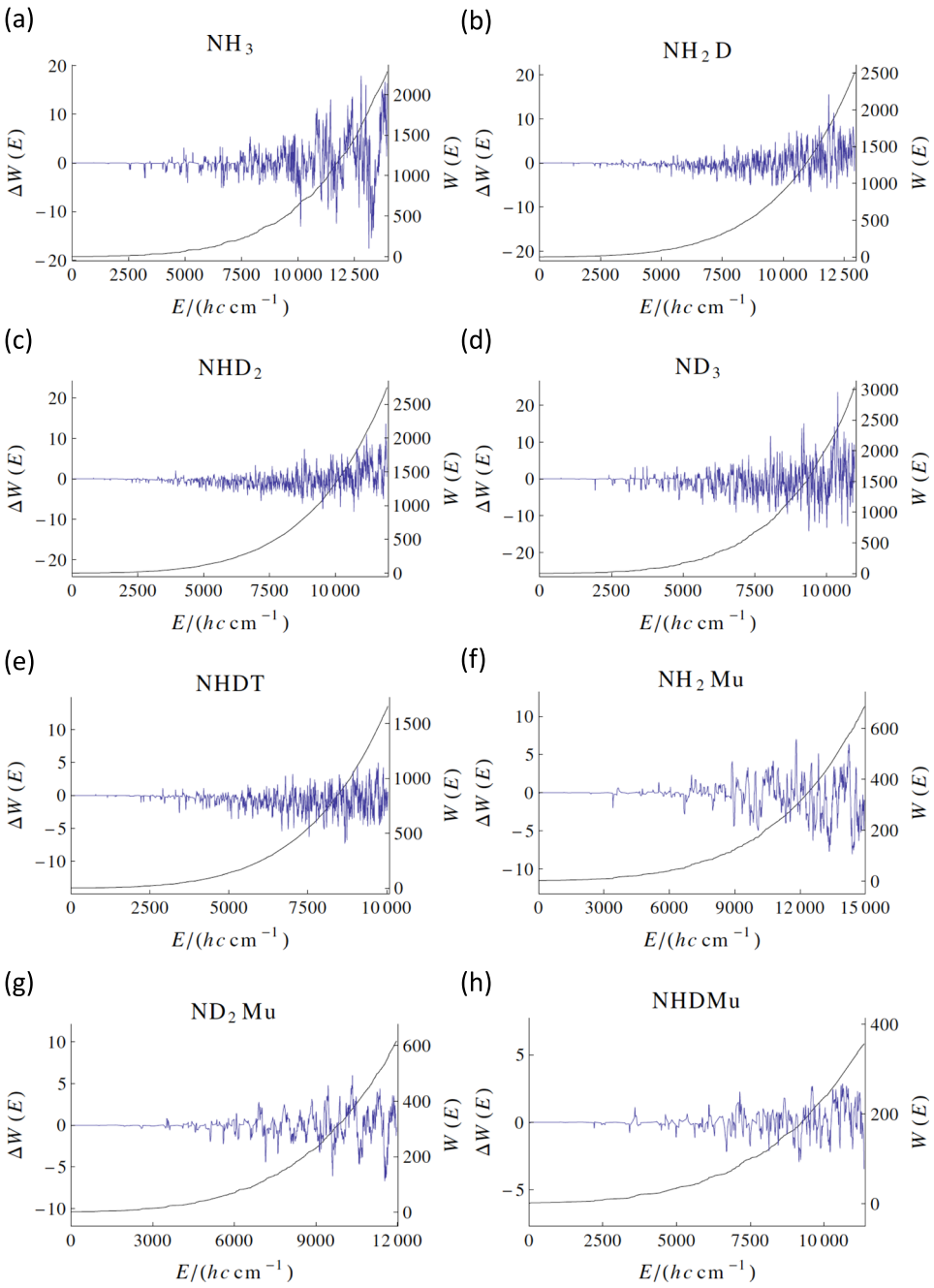


**FIG. 2**. Number of vibrational eigenstates $W(E)$ up to a given vibrational energy $E$ as a function of $E$ for selected $NH_3$ isotopomers (Mu refers to muonium, $\mu^+e^-$[140]). The black line gives the $W(E)$ function (ordinate on the right-hand side) for the AMMPOT4 PES, while the blue line depicts the difference $\Delta W(E) = W(E)_{\mathrm{AMMPOT4}} - W(E)_{\mathrm{NH3-Y2010}}$ (ordinate on the left-hand side) between the AMMPOT4 and NH3-Y2010 PES.

the ground-state and the fundamental quasiadiabatic channels. Fundamental channels are denoted by labels corresponding to the Mulliken convention, $\nu_i$ specifies a channel with one vibrational quantum in the vibrational mode $\nu_i$ and zero quanta in all other modes, except for the excited inversion sublevels. For the inversion degree of freedom, we introduce the label $v^{\pm}$, where $v$ means the number of inversion quanta and the labels +/− refer to the parity of a given vibrational eigenstate upon inversion at the planar ammonia structure. The VAR counterparts of the RPH energy levels can be identified by applying the overlap-based assignment techniques outlined in Sec. II C. The tunneling splittings given in Tables I–III reveal the mode specificity of tunneling; the consequences for the inhibition and enhancement of tunneling will be discussed in Sec. V. By comparing the VAR and RPH tunneling splittings, one can conclude that the RPH treatment

**TABLE I**. Variational (VAR) and quasiadiabatic-channel reaction-path Hamiltonian (RPH) vibrational energy levels ($E$), tunneling splittings ($\Delta E_{\pm}$), and irreducible representations ($\Gamma$) of the $S_2^*$ MS group for $NH_2D$. The ground-state (GS) and five fundamental channels are explicitly specified. The tunneling states $|v^{\pm}\rangle$ are characterized by the number of inversion quanta $v$ and parity (+/—).

| | | | $E/(hc\ \mathrm{cm}^{-1})$ | | $\Delta E_{\pm}/(hc\ \mathrm{cm}^{-1})$ | |
|---|---|---|---|---|---|---|
| Channel | State | $\Gamma$ | RPH | VAR | RPH | VAR |
| GS | $\|0^+\rangle$ | $A^+$ | 0.000 | 0.000 | | |
| | $\|0^-\rangle$ | $A^-$ | 0.291 | 0.382 | 0.291 | 0.382 |
| | $\|1^+\rangle$ | $A^+$ | 892.966 | 875.684 | | |
| | $\|1^-\rangle$ | $A^-$ | 909.168 | 894.699 | 16.201 | 19.015 |
| | $\|2^+\rangle$ | $A^+$ | 1556.837 | 1514.521 | | |
| | $\|2^-\rangle$ | $A^-$ | 1748.663 | 1734.846 | 191.826 | 220.325 |
| $\nu_6$ | $\|0^+\rangle$ | $B^+$ | 1441.418 | 1392.163 | | |
| | $\|0^-\rangle$ | $B^-$ | 1441.653 | 1392.620 | 0.234 | 0.457 |
| | $\|1^+\rangle$ | $B^+$ | 2352.707 | 2264.152 | | |
| | $\|1^-\rangle$ | $B^-$ | 2367.562 | 2286.721 | 14.854 | 22.569 |
| | $\|2^+\rangle$ | $B^+$ | 3022.923 | 2894.863 | | |
| | $\|2^-\rangle$ | $B^-$ | 3212.443 | 3125.116 | 189.520 | 230.253 |
| $\nu_3$ | $\|0^+\rangle$ | $A^+$ | 1648.054 | 1607.245 | | |
| | $\|0^-\rangle$ | $A^-$ | 1648.239 | 1590.762 | 0.184 | −16.483 |
| | $\|1^+\rangle$ | $A^+$ | 2575.127 | 2485.415 | | |
| | $\|1^-\rangle$ | $A^-$ | 2587.317 | 2483.930 | 12.190 | −1.485 |
| | $\|2^+\rangle$ | $A^+$ | 3267.628 | 3066.175 | | |
| | $\|2^-\rangle$ | $A^-$ | 3439.305 | 3347.421 | 171.677 | 281.246 |
| $\nu_2$ | $\|0^+\rangle$ | $A^+$ | 2588.618 | 2507.327 | | |
| | $\|0^-\rangle$ | $A^-$ | 2588.811 | 2507.180 | 0.193 | −0.147 |
| | $\|1^+\rangle$ | $A^+$ | 3499.268 | 3406.080 | | |
| | $\|1^-\rangle$ | $A^-$ | 3510.765 | 3417.861 | 11.497 | 11.781 |
| | $\|2^+\rangle$ | $A^+$ | 4195.585 | 4053.502 | | |
| | $\|2^-\rangle$ | $A^-$ | 4356.236 | 4237.242 | 160.651 | 183.740 |
| $\nu_1$ | $\|0^+\rangle$ | $A^+$ | 3516.828 | 3361.188 | | |
| | $\|0^-\rangle$ | $A^-$ | 3517.003 | 3365.242 | 0.175 | 4.053 |
| | $\|1^+\rangle$ | $A^+$ | 4432.022 | 4268.284 | | |
| | $\|1^-\rangle$ | $A^-$ | 4442.601 | 4296.928 | 10.578 | 28.643 |
| | $\|2^+\rangle$ | $A^+$ | 5136.867 | 4919.245 | | |
| | $\|2^-\rangle$ | $A^-$ | 5290.331 | 5097.807 | 153.464 | 178.561 |
| $\nu_5$ | $\|0^+\rangle$ | $B^+$ | 3628.990 | 3442.409 | | |
| | $\|0^-\rangle$ | $B^-$ | 3629.135 | 3442.673 | 0.145 | 0.264 |
| | $\|1^+\rangle$ | $B^+$ | 4552.558 | 4342.163 | | |
| | $\|1^-\rangle$ | $B^-$ | 4561.622 | 4352.332 | 9.064 | 10.169 |
| | $\|2^+\rangle$ | $B^+$ | 5272.860 | 5061.293 | | |
| | $\|2^-\rangle$ | $B^-$ | 5413.995 | 5193.779 | 141.135 | 132.486 |

**TABLE II**. Variational (VAR) and quasiadiabatic-channel reaction-path Hamiltonian (RPH) vibrational energy levels ($E$), tunneling splittings ($\Delta E_{\pm}$), and irreducible representations ($\Gamma$) of the $S_2^*$ MS group for $NHD_2$. The ground-state (GS) and five fundamental channels are explicitly specified. The tunneling states $|v^{\pm}\rangle$ are characterized by the number of inversion quanta $v$ and parity (+/—).

| | | | $E/(hc\ \mathrm{cm}^{-1})$ | | $\Delta E_{\pm}/(hc\ \mathrm{cm}^{-1})$ | |
|---|---|---|---|---|---|---|
| Channel | State | $\Gamma$ | RPH | VAR | RPH | VAR |
| GS | $\|0^+\rangle$ | $A^+$ | 0.000 | 0.000 | | |
| | $\|0^-\rangle$ | $A^-$ | 0.123 | 0.160 | 0.123 | 0.160 |
| | $\|1^+\rangle$ | $A^+$ | 824.029 | 808.808 | | |
| | $\|1^-\rangle$ | $A^-$ | 831.612 | 817.523 | 7.583 | 8.715 |
| | $\|2^+\rangle$ | $A^+$ | 1471.766 | 1449.683 | | |
| | $\|2^-\rangle$ | $A^-$ | 1592.212 | 1575.107 | 120.446 | 125.424 |
| $\nu_3$ | $\|0^+\rangle$ | $A^+$ | 1293.318 | 1234.286 | | |
| | $\|0^-\rangle$ | $A^-$ | 1293.421 | 1236.709 | 0.103 | 2.423 |
| | $\|1^+\rangle$ | $A^+$ | 2132.605 | 2080.452 | | |
| | $\|1^-\rangle$ | $A^-$ | 2139.752 | 2044.847 | 7.147 | −35.605 |
| | $\|2^+\rangle$ | $A^+$ | 2785.651 | 2648.113 | | |
| | $\|2^-\rangle$ | $A^-$ | 2906.247 | 2807.866 | 120.596 | 159.753 |
| $\nu_6$ | $\|0^+\rangle$ | $B^+$ | 1513.597 | 1461.482 | | |
| | $\|0^-\rangle$ | $B^-$ | 1513.669 | 1461.644 | 0.072 | 0.162 |
| | $\|1^+\rangle$ | $B^+$ | 2367.736 | 2280.208 | | |
| | $\|1^-\rangle$ | $B^-$ | 2373.002 | 2289.125 | 5.266 | 8.916 |
| | $\|2^+\rangle$ | $B^+$ | 3047.711 | 2928.776 | | |
| | $\|2^-\rangle$ | $B^-$ | 3148.153 | 3057.144 | 100.442 | 128.368 |
| $\nu_2$ | $\|0^+\rangle$ | $A^+$ | 2523.891 | 2435.420 | | |
| | $\|0^-\rangle$ | $A^-$ | 2523.983 | 2437.085 | 0.092 | 1.664 |
| | $\|1^+\rangle$ | $A^+$ | 3356.827 | 3263.652 | | |
| | $\|1^-\rangle$ | $A^-$ | 3362.726 | 3289.495 | 5.899 | 25.842 |
| | $\|2^+\rangle$ | $A^+$ | 4024.584 | 3929.716 | | |
| | $\|2^-\rangle$ | $A^-$ | 4128.070 | 4010.332 | 103.486 | 80.616 |
| $\nu_5$ | $\|0^+\rangle$ | $B^+$ | 2678.377 | 2564.108 | | |
| | $\|0^-\rangle$ | $B^-$ | 2678.439 | 2564.217 | 0.063 | 0.109 |
| | $\|1^+\rangle$ | $B^+$ | 3525.462 | 3387.591 | | |
| | $\|1^-\rangle$ | $B^-$ | 3529.687 | 3393.986 | 4.225 | 6.396 |
| | $\|2^+\rangle$ | $B^+$ | 4221.533 | 4071.591 | | |
| | $\|2^-\rangle$ | $B^-$ | 4305.047 | 4160.716 | 83.514 | 89.124 |
| $\nu_1$ | $\|0^+\rangle$ | $A^+$ | 3585.229 | 3406.314 | | |
| | $\|0^-\rangle$ | $A^-$ | 3585.291 | 3406.253 | 0.062 | −0.060 |
| | $\|1^+\rangle$ | $A^+$ | 4433.087 | 4230.812 | | |
| | $\|1^-\rangle$ | $A^-$ | 4437.293 | 4236.428 | 4.206 | 5.616 |
| | $\|2^+\rangle$ | $A^+$ | 5129.634 | 4915.945 | | |
| | $\|2^-\rangle$ | $A^-$ | 5213.146 | 5001.124 | 83.512 | 85.178 |

based on the adiabatic approximation clearly breaks down for some vibrational states. This breakdown, caused by nonadiabatic interactions between different channels, is indicated by substantial deviations (even two orders of magnitude in some extreme cases) between the VAR and RPH tunneling splittings, and it calls for an accurate variational treatment. One can also observe that the RPH and VAR tunneling splittings have opposite signs for some eigenstates. In the case of a one-dimensional tunneling model, it is possible to show that an even-parity energy level with $v^+$ is always lower than the corresponding odd-parity energy level with $v^-$. This statement does not apply to the VAR results where all couplings are treated in a numerically exact way. The situation in ammonia isotopomers is related to rather strong effects from intramolecular vibrational redistribution (IVR), which are much more pronounced than in the case of HOOH,[10,11] for example. It leads to some interesting observations when choosing a "quasiadiabatic channel state" as initial state.

**TABLE III**. Variational (VAR) and quasiadiabatic-channel reaction-path Hamiltonian (RPH) vibrational energy levels ($E$), tunneling splittings ($\Delta E_{\pm}$), and irreducible representations ($\Gamma$) of the $S^*$ MS group for NHDT. The ground-state (GS) and five fundamental channels are explicitly specified. The tunneling states $|v^{\pm}\rangle$ are characterized by the number of inversion quanta $v$ and parity (+/−).

| | | | $E/(hc\ \mathrm{cm}^{-1})$ | | $\Delta E_{\pm}/(hc\ \mathrm{cm}^{-1})$ | |
|---|---|---|---|---|---|---|
| Channel | State | $\Gamma$ | RPH | VAR | RPH | VAR |
| GS | $\|0^+\rangle$ | $A^+$ | 0.000 | 0.000 | | |
| | $\|0^-\rangle$ | $A^-$ | 0.087 | 0.114 | 0.087 | 0.114 |
| | $\|1^+\rangle$ | $A^+$ | 795.667 | 778.925 | | |
| | $\|1^-\rangle$ | $A^-$ | 801.219 | 785.108 | 5.552 | 6.183 |
| | $\|2^+\rangle$ | $A^+$ | 1435.686 | 1408.227 | | |
| | $\|2^-\rangle$ | $A^-$ | 1533.112 | 1517.544 | 97.427 | 109.317 |
| $\nu_5$ | $\|0^+\rangle$ | $A^+$ | 1201.134 | 1152.289 | | |
| | $\|0^-\rangle$ | $A^-$ | 1201.211 | 1154.455 | 0.077 | 2.166 |
| | $\|1^+\rangle$ | $A^+$ | 2008.260 | 1857.500 | | |
| | $\|1^-\rangle$ | $A^-$ | 2013.695 | 1924.495 | 5.435 | 66.995 |
| | $\|2^+\rangle$ | $A^+$ | 2650.306 | 2513.372 | | |
| | $\|2^-\rangle$ | $A^-$ | 2750.217 | 2661.349 | 99.912 | 147.977 |
| $\nu_4$ | $\|0^+\rangle$ | $A^+$ | 1484.448 | 1441.156 | | |
| | $\|0^-\rangle$ | $A^-$ | 1484.499 | 1431.423 | 0.051 | −9.733 |
| | $\|1^+\rangle$ | $A^+$ | 2308.801 | 2224.202 | | |
| | $\|1^-\rangle$ | $A^-$ | 2312.614 | 2217.352 | 3.813 | −6.851 |
| | $\|2^+\rangle$ | $A^+$ | 2980.203 | 2841.121 | | |
| | $\|2^-\rangle$ | $A^-$ | 3060.041 | 2968.245 | 79.838 | 127.124 |
| $\nu_3$ | $\|0^+\rangle$ | $A^+$ | 2172.207 | 2110.904 | | |
| | $\|0^-\rangle$ | $A^-$ | 2172.268 | 2111.016 | 0.061 | 0.112 |
| | $\|1^+\rangle$ | $A^+$ | 2978.094 | 2899.705 | | |
| | $\|1^-\rangle$ | $A^-$ | 2982.142 | 2901.507 | 4.048 | 1.802 |
| | $\|2^+\rangle$ | $A^+$ | 3641.331 | 3567.223 | | |
| | $\|2^-\rangle$ | $A^-$ | 3720.844 | 3639.629 | 79.514 | 72.406 |
| $\nu_2$ | $\|0^+\rangle$ | $A^+$ | 2617.165 | 2516.176 | | |
| | $\|0^-\rangle$ | $A^-$ | 2617.214 | 2516.321 | 0.049 | 0.145 |
| | $\|1^+\rangle$ | $A^+$ | 3431.613 | 3310.753 | | |
| | $\|1^-\rangle$ | $A^-$ | 3435.001 | 3308.075 | 3.388 | −2.678 |
| | $\|2^+\rangle$ | $A^+$ | 4110.156 | 3989.339 | | |
| | $\|2^-\rangle$ | $A^-$ | 4180.820 | 4047.864 | 70.664 | 58.526 |
| $\nu_1$ | $\|0^+\rangle$ | $A^+$ | 3580.545 | 3403.448 | | |
| | $\|0^-\rangle$ | $A^-$ | 3580.588 | 3403.328 | 0.043 | −0.121 |
| | $\|1^+\rangle$ | $A^+$ | 4396.429 | 4198.484 | | |
| | $\|1^-\rangle$ | $A^-$ | 4399.402 | 4200.264 | 2.974 | 1.780 |
| | $\|2^+\rangle$ | $A^+$ | 5081.540 | 4880.772 | | |
| | $\|2^-\rangle$ | $A^-$ | 5145.734 | 4938.494 | 64.194 | 57.722 |

## IV. QUANTUM MOLECULAR DYNAMICS RESULTS

### A. Quantum dynamics for the achiral $NHD_2$ and the chiral NHDT isotopomers

The eigenstate computations described in Sec. III are not only useful for obtaining rovibrational energy levels and eigenstates and comparing different PES, but more importantly also provide the starting point for our time-dependent quantum-dynamical computations. In order to study the coherent inhibition and enhancement of tunneling in $NHD_2$ and NHDT, we computed around 16 000 rovibrational eigenstates for both isotopomers. These eigenstates cover the $J = 0$–7 rotational quantum number range, and the corresponding rovibrational term values extend to about 6000 $\mathrm{cm}^{-1}$ above the zero-point term value for both isotopomers. The time-independent methodological developments outlined in Sec. II B are crucial for the computation of these large rovibrational eigenstate bases which are then used to represent the TDSE as discussed in Sec. II D.

The choice of the two isotopomers $NHD_2$ and NHDT can be justified by the following arguments: (a) the tunneling dynamics of the achiral isotopomer $NHD_2$ has already been examined by a series of vibration-only studies,[77–79,82,83] which are now complemented by our rovibrational study; (b) NHDT, although its quantum dynamics has not been investigated by any theoretical studies so far, is chiral and its stereomutation corresponds to a prototypical enantiomerisation reaction. In principle, NHDT shows effects from parity violation, which, however, can be safely neglected here, because the tunneling splittings are many orders of magnitude larger than the parity violating potentials in this isotopically chiral molecule.[110,141]

The key feature of our work is that, in contrast to the majority of time-dependent quantum-dynamical studies carried out for molecules so far, not only the vibrational but also the rotational degrees of freedom and their couplings are included. The consequences of disregarding the rotational degrees of freedom were analyzed in detail by studies focusing on the rovibrational quantum dynamics of HF during infrared multiphoton excitation.[142,143] There, it was concluded that, under certain circumstances, the excitation dynamics converges to that of the vibration-only model (neglecting the rotational degrees of freedom and assuming that the time-dependent electric field is parallel to the axis of HF), called "pure vibrational model" in Ref. 143. The rotational degrees of freedom are also of great relevance in the theory of light-induced conical intersections.[144–147]

Throughout Secs. IV A–IV D describing time-dependent results, the initial state has been defined as

$$\Psi(t=0) = \frac{1}{\sqrt{2}}(\Phi_+ + \Phi_-), \tag{52}$$

where $\Phi_+$ and $\Phi_-$ are the symmetric and antisymmetric components of the vibrational ground state. $\Psi(t = 0)$ corresponds to a "classical-like" state localized in one of the potential wells (see Ref. 148 and the corresponding discussion in Ref. 149 for this initial state in ammonia and more generally also in chiral molecules). The periodic time evolution of this localized initial state under field-free conditions is governed by the tunneling splitting $\Delta E_{\pm}$ with a time period of $\tau = h/|\Delta E_{\pm}|$, as already derived in Eq. (39). The corresponding time-dependent probability density reads as

$$P(t) = \frac{1}{2}\Big(|\Phi_+|^2 + |\Phi_-|^2 + \Phi_+^*\Phi_- \exp(-\mathrm{i}2\pi\Delta E_{\pm}t/h) + \Phi_+\Phi_-^* \exp(\mathrm{i}2\pi\Delta E_{\pm}t/h)\Big), \tag{53}$$

where $\Delta E_{\pm} = E_- - E_+$. The AMMPOT4 ground-state tunneling splittings obtained by 6D GENIUSH computations are

$\Delta E_{\pm} = 0.160\ cm^{-1}$ for $NHD_2$ and $\Delta E_{\pm} = 0.114\ cm^{-1}$ for NHDT, and the corresponding field-free tunneling periods are $\tau = 208.9$ ps and $\tau = 292.8$ ps, respectively.

The solution of the TDSE results in complex probability amplitudes $b_k(t)$ and real populations $p_k(t) = |b_k(t)|^2$ for the rovibrational eigenstates included in the eigenstate basis. Two further quantities of interest are the full-dimensional and the reduced probability densities

$$P(\mathbf{Q}, t) = |\Psi(\mathbf{Q}, t)|^2,$$
$$P_{red}(\mathbf{q}, t) = \int P(\mathbf{q}, \mathbf{q}', t) d\mathbf{q}', \quad (54)$$

where $\mathbf{Q}$ is a vector of the nuclear coordinates. In the reduced case, $\mathbf{Q}$ is divided into two sets of coordinates (denoted by $\mathbf{q}$ and $\mathbf{q}'$) and $P(\mathbf{Q}, t)$ is integrated over all possible values of $\mathbf{q}'$. If one is interested in describing the inversion motion of ammonia isotopomers, the case of the present study, an obvious choice for $P_{red}(\mathbf{q}, t)$ is defined by integrating $P(\mathbf{Q}, t)$ over all coordinates but the inversion coordinate (the azimuthal angle $\varphi$ in the particular case of Radau coordinates), yielding what is called the inversion probability density. In addition to the inversion density, for $NH_3$ isotopomers, it is useful to define the time-dependent quantity

$$P_R(t) = \int_R P(\mathbf{Q}, t) d\mathbf{Q}, \quad (55)$$

where the integration is carried out for a selected half of the configuration space corresponding to one of the two enantiomeric subspaces (or "potential wells"). In the specific case of Radau coordinates used in this study for ammonia, the region R is defined as $0° \le \varphi \le 180°$, and $P_R(t)$ reveals to what extent the wavepacket is localized in the selected subspace. Finally, the revival probability $p_{rev}(t) = |\langle\Psi(0)|\Psi(t)\rangle|^2$ also provides valuable information about the dynamics. For the chiral isotopomer NHDT, the integration provides the probability $P(K, t)$ for each enantiomer with K = R or S.

For the practical application of the tunneling inhibition[122] and enhancement[124] strategies summarized in Sec. II F, we first investigate a compact eigenstate space that we expect to play an important role in the dynamics. For this selected space, we use the Floquet approach described in Sec. II F to deduce appropriate laser parameters. The feasibility of the thus designed dynamical schemes will then be demonstrated by accurate time-dependent computations in the 16 000-dimensional eigenstate basis described in the first paragraph of this section. The use of compact eigenstate spaces is restricted to sufficiently low laser intensities. One case, where this approximate treatment breaks down spectacularly, will be presented in Sec. IV B.

**TABLE IV**. List of eigenstates $|v^{\pm}, JK_aK_c\rangle$ relevant for the tunneling inhibition and enhancement schemes for $NHD_2$ and NHDT, characterized by the number of inversion quanta $v$, vibrational parity (+ or −, in superscript), and the ($J$, $K_a$, $K_c$) rotational quantum numbers. Symmetry labels ($\Gamma$) for the MS groups $S_2^*$ ($NHD_2$) and $S^*$ (NHDT) and energy levels ($E$) are given explicitly.

| $NHD_2$ | | | NHDT | | |
|---|---|---|---|---|---|
| State | $\Gamma$ | $E/(hc\ cm^{-1})$ | State | $\Gamma$ | $E/(hc\ cm^{-1})$ |
| $\|0^+, 000\rangle$ | $A^+$ | 0.000 | $\|0^+, 000\rangle$ | $A^+$ | 0.000 |
| $\|0^-, 000\rangle$ | $A^-$ | 0.160 | $\|0^-, 000\rangle$ | $A^-$ | 0.114 |
| $\|1^+, 101\rangle$ | $B^-$ | 817.795 | $\|1^+, 101\rangle$ | $A^-$ | 786.303 |
| $\|1^+, 111\rangle$ | $A^-$ | 819.992 | $\|1^+, 111\rangle$ | $A^-$ | 789.104 |
| $\|1^+, 110\rangle$ | $A^+$ | 821.591 | $\|1^+, 110\rangle$ | $A^+$ | 790.252 |
| $\|1^-, 101\rangle$ | $B^+$ | 826.508 | $\|1^-, 101\rangle$ | $A^+$ | 792.491 |
| $\|1^-, 111\rangle$ | $A^+$ | 828.677 | $\|1^-, 111\rangle$ | $A^+$ | 795.266 |
| $\|1^-, 110\rangle$ | $A^-$ | 830.249 | $\|1^-, 110\rangle$ | $A^-$ | 796.404 |

**TABLE V**. Nonzero electric dipole moment matrix elements $\mu_{ij}$ relevant for the tunneling inhibition and enhancement schemes for $NHD_2$. The eigenstates $|v^{\pm}, JK_aK_c\rangle$ are characterized by the number of inversion quanta $v$, vibrational parity (+ or −, in superscript), and the ($J$, $K_a$, $K_c$) rotational quantum numbers.

| $\mu_{ij}$/D | $\|0^+, 000\rangle$ | $\|0^-, 000\rangle$ |
|---|---|---|
| $\|1^+, 101\rangle$ | | |
| $\|1^+, 111\rangle$ | $3.74 \cdot 10^{-2}$ | |
| $\|1^+, 110\rangle$ | | $1.10 \cdot 10^{-1}$ |
| $\|1^-, 101\rangle$ | | |
| $\|1^-, 111\rangle$ | | $3.45 \cdot 10^{-2}$ |
| $\|1^-, 110\rangle$ | $-1.06 \cdot 10^{-1}$ | |

We use the notation $|v^{\pm}, JK_aK_c\rangle$ to label the eigenstates relevant for our study, where $v$ is the number of vibrational quanta in the inversion mode (the other "good" vibrational quantum numbers are zero for the eigenstates selected), the superscripts + and − specify the parity with respect to the inversion mode, and $(J, K_a, K_c)$ denote the well-known rotational quantum numbers for a rigid-rotor asymmetric top.[150] Although ammonia and its isotopomers are nonrigid molecules, the rotational increments (differences between the rovibrational energy levels and their vibrational parent energy levels) are close to the rigid-rotor energy levels for the eigenstates in Table IV; therefore, it is meaningful to apply the conventional rigid-rotor quantum numbers to label the eigenstates. In addition to the eigenstates $|0^+, 000\rangle$ and $|0^-, 000\rangle$, denoted by $\Phi_+$ and $\Phi_-$ in Eq. (52), we have chosen the six eigenstates $|1^{\pm}, 1K_aK_c\rangle$. The energy-level values corresponding to the selected eigenstates and their symmetry labels $\Gamma$ are summarized in Table IV for $NHD_2$ and NHDT, where the $S_2^*$ and

**TABLE VI**. Nonzero electric dipole moment matrix elements $\mu_{ij}$ relevant for the tunneling inhibition and enhancement schemes for NHDT. The eigenstates $|v^{\pm}, JK_aK_c\rangle$ are characterized by the number of inversion quanta $v$, vibrational parity (+ or −, in superscript), and the ($J$, $K_a$, $K_c$) rotational quantum numbers.

| $\mu_{ij}$/D | $\|0^+, 000\rangle$ | $\|0^-, 000\rangle$ |
|---|---|---|
| $\|1^+, 101\rangle$ | $-2.34 \cdot 10^{-2}$ | |
| $\|1^+, 111\rangle$ | $-4.05 \cdot 10^{-2}$ | |
| $\|1^+, 110\rangle$ | | $1.04 \cdot 10^{-1}$ |
| $\|1^-, 101\rangle$ | | $1.88 \cdot 10^{-2}$ |
| $\|1^-, 111\rangle$ | | $3.72 \cdot 10^{-2}$ |
| $\|1^-, 110\rangle$ | $-1.00 \cdot 10^{-1}$ | |

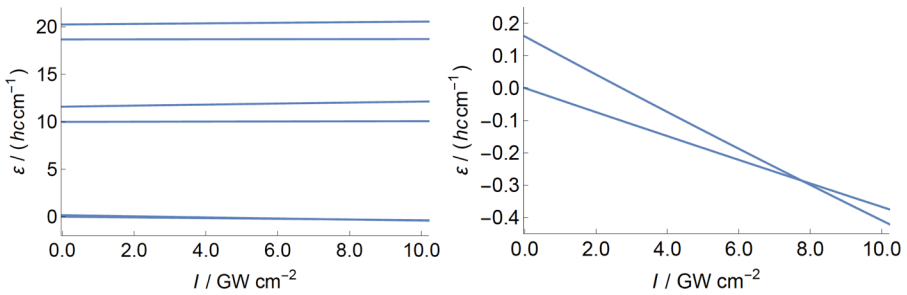


**FIG. 3**. Selected $NHD_2$ quasienergy diagrams for the tunneling inhibition scheme shown as a function of the intensity $I$ ($\tilde{\nu}_0 = 810\,\mathrm{cm}^{-1}$). The two lowest quasienergy lines on the left panel cross at $I$ = 7.77 GW cm$^{-2}$, highlighted on the right panel.

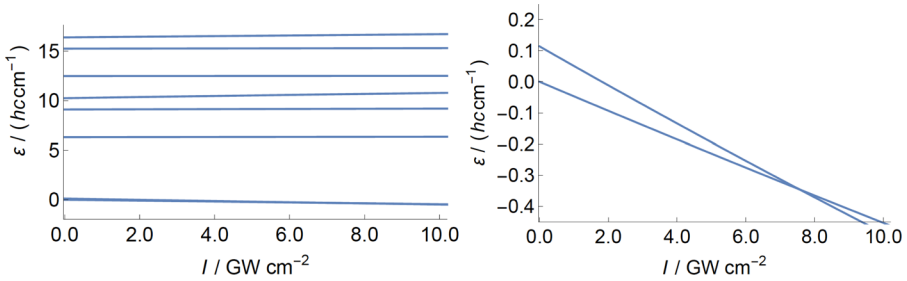


**FIG. 4**. Selected NHDT quasienergy diagrams for the tunneling inhibition scheme shown as a function of the intensity $I$ ($\tilde{\nu}_0 = 780\,\mathrm{cm}^{-1}$). The two lowest quasienergy lines on the left panel cross at $I$ = 7.56 GW cm$^{-2}$, highlighted on the right panel.

S* MS groups[110,151] are used for $NHD_2$ and NHDT, respectively. Furthermore, because we neglect hyperfine interactions and sublevels, the nuclear-spin symmetry is conserved for $NHD_2$ in the radiative couplings (A or B). As the electric dipole moment operator $\boldsymbol{\mu}_{el}$ transforms according to the irreducible representation $A^-$ for both MS groups, the initial state in Eq. (52) is allowed to couple to eigenstates of $A^+$ and $A^-$ symmetries by $\boldsymbol{\mu}_{el}$. In addition to this simple rule, it is important to state explicitly that the eigenstates $|0^+, 000\rangle$ and $|0^-, 000\rangle$ are allowed to couple to J = 1 eigenstates (angular momentum selection rule). Moreover, as we work with linearly polarized light, the angular momentum projection quantum number M is conserved. As the initial state in Eq. (52) is a linear combination of J = 0 eigenstates, the M = 0 condition remains valid throughout the dynamics due to the conservation of M. The electric dipole matrix elements $\mu_{ij}$ between the selected eigenstates are summarized in Tables V and VI. One can observe that only six eigenstates are involved in the

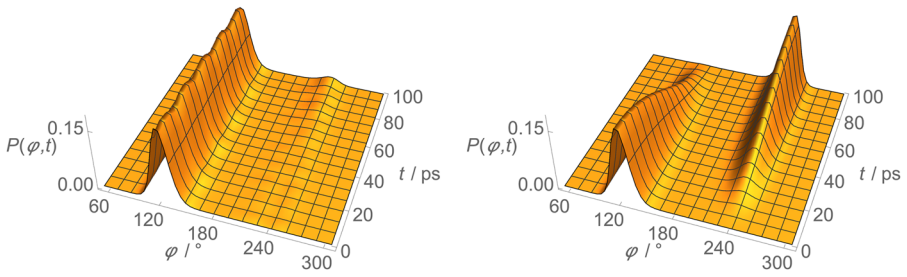


**FIG. 5**. Reduced probability density as a function of the inversion coordinate $\varphi$ and time $t$ for $NHD_2$. The left and right panels show reduced probability densities (probability densities integrated over all other coordinates) for the tunneling inhibition and field-free dynamical schemes, respectively. The laser parameters are $\tilde{\nu}_0 = 810\,\mathrm{cm}^{-1}$ and $I$ = 7.77 GW cm$^{-2}$.

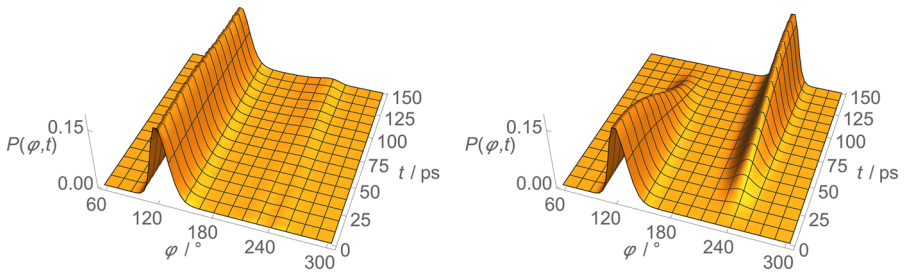


**FIG. 6**. Reduced probability density as a function of the inversion coordinate $\varphi$ and time $t$ for NHDT. The left and right panels show reduced probability densities (probability densities integrated over all other coordinates) for the tunneling inhibition and field-free dynamical schemes, respectively. The laser parameters are $\tilde{\nu}_0 = 780\,\mathrm{cm}^{-1}$ and $I$ = 7.56 GW cm$^{-2}$.

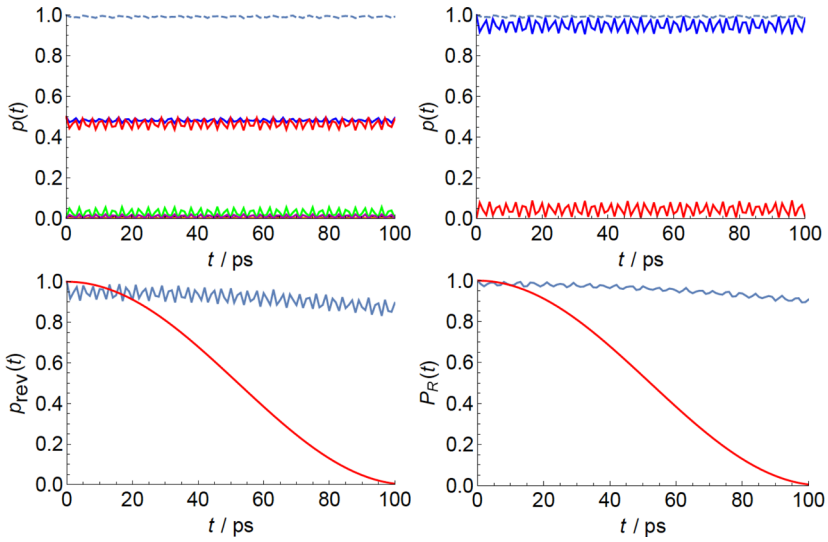


**FIG. 7.** Populations of selected eigenstates (upper left panel— $|0^+,000\rangle$: blue, $|0^-,000\rangle$: red, $|1^+,111\rangle$: black, $|1^+,110\rangle$: green, $|1^-,111\rangle$: orange, $|1^-,110\rangle$: magenta, sum of the six populations: blue dashed line) and coarse-grained populations in $J$ (upper right panel—$J$ = 0: blue, $J$ = 1: red, sum of the $J$ = 0 and $J$ = 1 coarse-grained populations: blue dashed line) as a function of time $t$ for the tunneling inhibition scheme for $NHD_2$. The lower left and right panels show $p_{rev}(t) = |\langle\Psi(0)|\Psi(t)\rangle|^2$ and $P_R(t)$ (tunneling inhibition scheme: blue, field-free dynamics: red), respectively. The laser parameters are $\tilde{\nu}_0 = 810\,\mathrm{cm}^{-1}$ and $I = 7.77\ \mathrm{GW\ cm}^{-2}$.

dynamics for $NHD_2$ due to its higher symmetry. The energy levels, eigenstates, and $\mu_{ij}$ matrix elements were computed with the AMMPOT4 PES and the DMS of Ref. 15. Our choice of the eigenstate space can be justified by noting the following: (a) the eigenstate space is compact (six states for $NHD_2$ and eight states for NHDT); (b) the $J = 1$ energy levels form a cluster which is well isolated from other energy levels. In the following paragraphs, we describe how the laser parameters of the tunneling inhibition and enhancement schemes can be designed by employing the selected compact eigenstate spaces and the Floquet approach described in Sec. II F. Common to both dynamical schemes is the application of linearly-polarized off-resonant laser fields. The laser intensities used in this work are orders of magnitude smaller than the threshold ionization intensity, estimated to be 40 TW $\mathrm{cm}^{-2}$, for $NHD_2$.[77]

## B. Tunneling inhibition

According to Sec. II F, the coherent inhibition of tunneling is achieved by continuous-wave excitations that give rise to quasienergy crossings. We have found that for the laser parameters $\tilde{\nu}_0 = 810\ \mathrm{cm}^{-1}$ and $I = 7.77\ \mathrm{GW\ cm}^{-2}$ ($NHD_2$), as well as $\tilde{\nu}_0 = 780\ \mathrm{cm}^{-1}$ and $I = 7.56\ \mathrm{GW\ cm}^{-2}$ (NHDT), the localized initial state $\Psi(t = 0)$ can be described, to a very good approximation, as a superposition of two Floquet states with coincident quasienergies; therefore, $\Psi(t = 0)$ will remain localized in the initially occupied potential well. The quasienergy lines

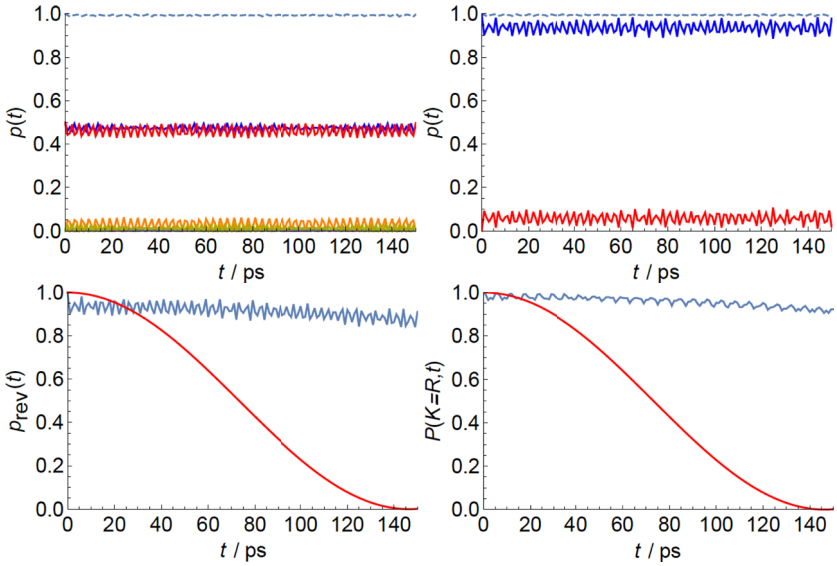


**FIG. 8.** Populations of selected eigenstates (upper left panel—$|0^+,000\rangle$: blue, $|0^-,000\rangle$: red, $|1^+,101\rangle$: black, $|1^+,111\rangle$: green, $|1^+,110\rangle$: orange, $|1^-,101\rangle$: magenta, $|1^-,111\rangle$: gray, $|1^-,110\rangle$: yellow, sum of the eight populations: blue dashed line) and coarse-grained populations in $J$ (upper right panel—$J$ = 0: blue, $J$ = 1: red, sum of the $J$ = 0 and $J$ = 1 coarse-grained populations: blue dashed) as a function of time $t$ for the tunneling inhibition scheme for NHDT. The lower left and right panels show $p_{rev}(t) = |\langle\Psi(0)|\Psi(t)\rangle|^2$ and $P(K = R, t)$ (tunneling inhibition scheme: blue, field-free dynamics: red), respectively. The laser parameters are $\tilde{\nu}_0 = 780\,\mathrm{cm}^{-1}$ and $I = 7.56\ \mathrm{GW\ cm}^{-2}$.

given as a function of the laser intensity at the selected excitation wavenumbers $\tilde{\nu}_0$ are displayed in Figs. 3 and 4, where the right panels magnify the quasienergy ranges where the exact crossings of the quasienergy lines occur, allowed by the opposite generalized parities of the two Floquet states involved. As the laser parameters needed for the coherent inhibition of tunneling stem from reduced six-state ($NHD_2$) and eight-state (NHDT) models, it is necessary to prove the validity of the parameters using numerically exact quantum-dynamical computations. The dimensionless inversion densities ($P(\varphi, t)/(1/^\circ)$) expressed as a function of the azimuthal angle $\varphi$ and shown in Fig. 5 ($NHD_2$) and Fig. 6 (NHDT) reveal that in contrast to the field-free case the wave function remains localized in the initial well as a result of the laser excitation. This conclusion is also confirmed by Figs. 7 and 8, where populations of selected eigenstates, coarse-grained populations in J (sum of all eigenstate populations for a given J value), $p_{rev}(t)$, $P_R(t)$ ($NHD_2$), and P(K = R, t) (NHDT) are given.

The eigenstate populations show small-amplitude oscillations and only a small amount of population is transferred to the J = 1 eigenstates over the course of the laser excitation; this is due to the off-resonant conditions. Figures 7 and 8 also reveal that there is virtually no population leak from the six-state ($NHD_2$) and eight-state (NHDT) eigenstate spaces used to design the laser parameters. This observation confirms that the six- and eight-state models provide reliable results in the intensity range applied. The $p_{rev}(t)$, $P_R(t)$ ($NHD_2$), and P(K = R, t) (NHDT) functions shown in Figs. 7 and 8 remain close to their initial values of 1.0 in the case of driven tunneling, and therefore they also support our conclusion. Regarding the robustness of the scheme described, the degree of tunneling inhibition is virtually unaltered by a 1 $cm^{-1}$ change in $\tilde{\nu}_0$ and a 10% change in I for the time scale investigated. Finally, we note that the excitation wavenumber of $\tilde{\nu}_0 = 810\,cm^{-1}$ chosen for $NHD_2$ is similar to one of the values used by the vibration-only study of Ref. 83.

We have also identified a second quasienergy line crossing predicted by the eight-state model for NHDT, and the corresponding laser parameters are $\tilde{\nu}_0 = 720\,cm^{-1}$ and $I = 0.152$ TW $cm^{-2}$. Compared to the coherent inhibition parameters proposed for NHDT earlier in this section, it is easy to see that a higher intensity is needed at $\tilde{\nu}_0 = 720\,cm^{-1}$ than at $\tilde{\nu}_0 = 780\,cm^{-1}$ to maintain localization in the initial well. Although the eight-state model predicts tunneling inhibition, the coarse-grained populations in J and in E shown in Fig. 9, both obtained by numerically exact computations, clearly indicate that a substantial population transfer takes place to eigenstates that are not included in the eight-state subspace defined in Table IV. Therefore, the eight-state model is not applicable in this case and one has to include several other eigenstates to evaluate quasienergies and locate their crossings.

### C. Tunneling enhancement

The coherent enhancement of tunneling has been achieved in this study by applying off-resonant laser pulses with the smooth envelope function $f(t) = \sin^2(\pi t/t_p)$, where $t_p$ characterizes the length of the laser pulse. The parameters $\tilde{\nu}_0 = 825.0\,cm^{-1}$, $I_{max} = 5.85$ GW $cm^{-2}$, $t_p = 25$ ps ($NHD_2$), and $\tilde{\nu}_0 = 793.5\,cm^{-1}$, $I_{max} = 3.15$ GW $cm^{-2}$, $t_p = 40$ ps (NHDT) have been found to transfer the population from the initial well to the other well faster than the respective field-free tunneling times. Figure 10 clearly shows that the two quasienergy lines, correlated with the eigenstates $|\Phi_+\rangle = |0^+, 000\rangle$ and $|\Phi_-\rangle = |0^-, 000\rangle$, repel each other as the intensity of the laser increases, giving rise to the enhancement of tunneling according to Sec. II F. The inversion densities shown in Figs. 11 and 12 clearly manifest the enhancement of tunneling compared to the field-free case. The effect of weak population transfer to the $|1^\pm, 1K_aK_c\rangle$ eigenstates is visible around $t = t_p/2$, as shown by the two adjacent lobes appearing in the inversion density plots. This observation is further verified by the eigenstate populations displayed in Figs. 13 and 14, showing that the J = 1 eigenstates of Table IV are populated only transiently, and the eigenstate populations return to their initial values at the end of the laser pulse, which is in accordance with the adiabatic Floquet theory. The $p_{rev}(t)$, $P_R(t)$ ($NHD_2$), and P(K = R, t) (NHDT) functions, also shown in Figs. 13 and 14, approach zero at the end of the pulse, indicating that the laser pulse has induced a 180° shift in the relative phase between $\Phi_+$ and $\Phi_-$. In other words, the tunneling process has occurred and the initial state $(\Phi_+ + \Phi_-)/\sqrt{2}$ has

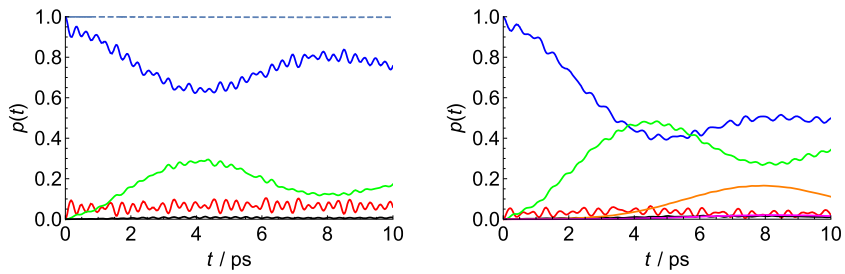


**FIG. 9.** Coarse-grained populations in J (left panel—J = 0: blue, J = 1: red, J = 2: green, J = 3: black, sum of the J = 0, J = 1, J = 2, and J = 3 coarse-grained populations: blue dashed line) and in E (right panel—$E/(hc)$ = 0–360 $cm^{-1}$: blue, $E/(hc)$ = 360–1080 $cm^{-1}$: red, $E/(hc)$ = 1080–1800 $cm^{-1}$: green, $E/(hc)$ = 1800–2520 $cm^{-1}$: black, $E/(hc)$ = 2520–3240 $cm^{-1}$: orange, $E/(hc)$ > 3240 $cm^{-1}$: magenta) for NHDT. The laser parameters are chosen as $\tilde{\nu}_0 = 720\,cm^{-1}$ and $I = 0.152$ TW $cm^{-2}$.

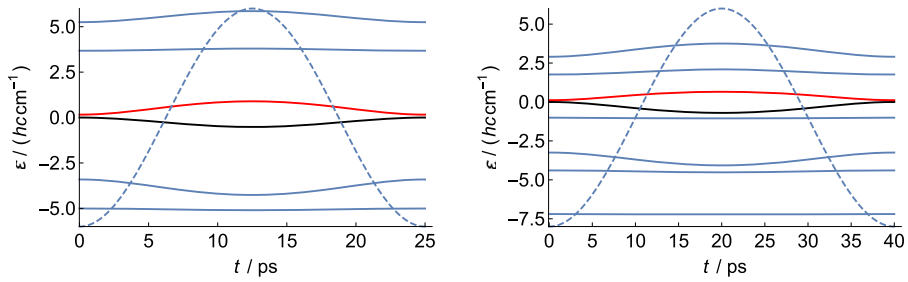


**FIG. 10**. Selected quasienergy diagrams for the tunneling enhancement scheme as a function of time $t$ over the course of the laser pulse ($NHD_2$: left panel—$\tilde{\nu}_0 = 825.0\,\mathrm{cm}^{-1}$, $I_{max}$ = 5.85 GW cm$^{-2}$, and $t_p$ = 25 ps; NHDT: right panel—$\tilde{\nu}_0 = 793.5\,\mathrm{cm}^{-1}$, $I_{max}$ = 3.15 GW cm$^{-2}$, and $t_p$ = 40 ps). The black and red lines show quasienergy lines correlated with the eigenstates $|0^+, 000\rangle$ and $|0^-, 000\rangle$, respectively. The envelope function [$f(t) = \sin^2(\pi t/t_p)$] of the laser pulse is indicated by the blue dashed line.

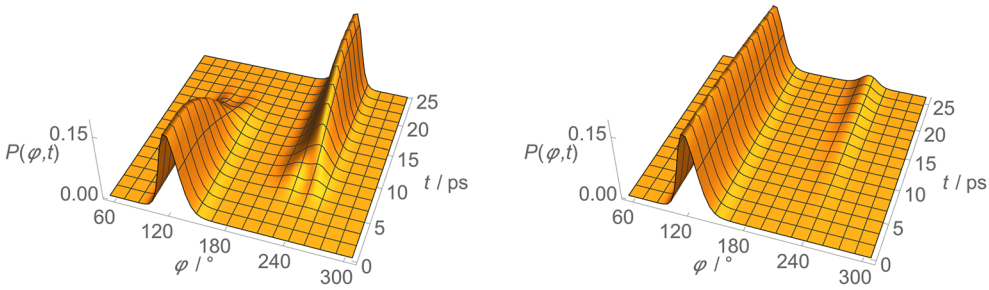


**FIG. 11**. Reduced probability density as a function of the inversion coordinate $\varphi$ and time $t$ for $NHD_2$. The left and right panels show reduced probability densities (probability densities integrated over all other coordinates) for the tunneling enhancement and field-free dynamical schemes, respectively. The parameters of the laser pulse are $\tilde{\nu}_0 = 825.0\,\mathrm{cm}^{-1}$, $I_{max}$ = 5.85 GW cm$^{-2}$, and $t_p$ = 25 ps.

become $(\Phi_+ - \Phi_-)/\sqrt{2}$ (apart from an extra phase). Comparing the pulse lengths of $t_p$ = 25 ps ($NHD_2$) and $t_p$ = 40 ps (NHDT) to the respective field-free tunneling times $\tau/2$ = 104.5 ps and $\tau/2$ = 146.4 ps indicates an approximately four-fold acceleration of tunneling with respect to the field-free case. We stress that the driving wavenumbers were chosen in such a way that an optimal separation between the quasienergy lines of the same generalized parity is achieved, which is vital for maintaining adiabatic conditions in addition to choosing a sufficiently long laser pulse with a smooth envelope function. The tunneling enhancement scheme is stable with respect to a few percent fluctuation in $I_{max}$ at the $\tilde{\nu}_0$ values reported.

### D. Results on flux associated with coherent tunneling in $NH_3$

In addition to the time-dependent results on driven tunneling, we have also investigated the nuclear-motion flux associated with coherent tunneling in $NH_3$ for the field-free case. For this purpose, we have abandoned the Radau coordinates used in other parts of this study and computed vibrational eigenstates in terms of the internal coordinates defined in Table IV of Ref. 73. The particular advantage of this choice is that the inversion motion is described by an inversion angle $\theta$ ranging from 0° to 180°. This definition facilitates the comparison of our results to the ones published in Refs. 90, 91, and 93.

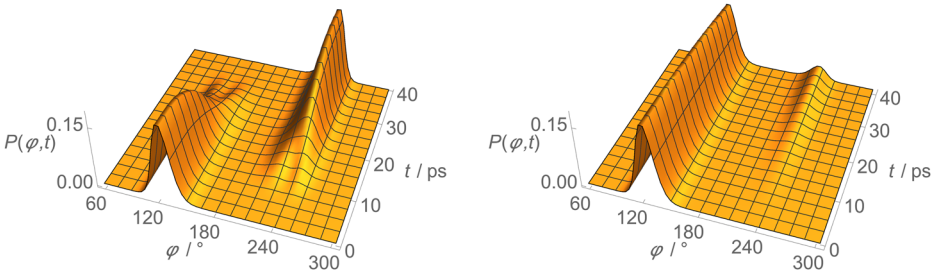


**FIG. 12**. Reduced probability density as a function of the inversion coordinate $\varphi$ and time $t$ for NHDT. The left and right panels show reduced probability densities (probability densities integrated over all other coordinates) for the tunneling enhancement and field-free dynamical schemes, respectively. The parameters of the laser pulse are $\tilde{\nu}_0 = 793.5\,\mathrm{cm}^{-1}$, $I_{max}$ = 3.15 GW cm$^{-2}$, and $t_p$ = 40 ps.

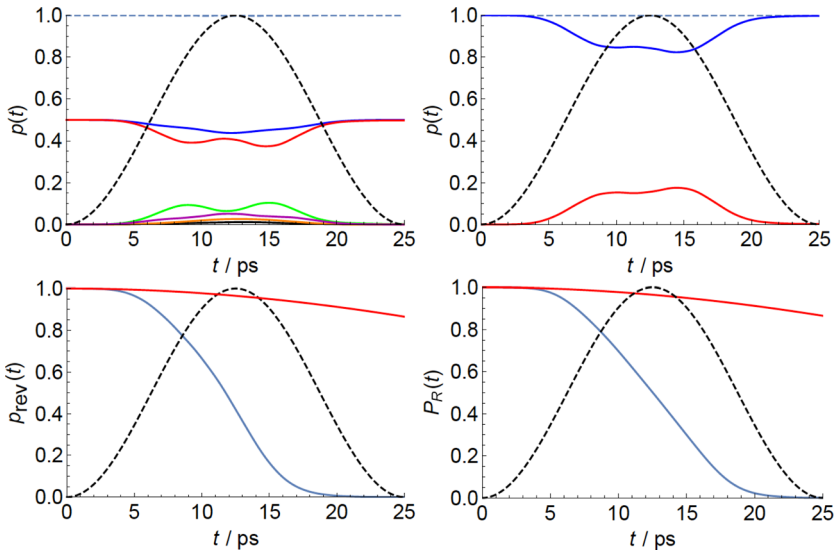


**FIG. 13**. Populations of selected eigenstates (upper left panel—$|0^+,000\rangle$: blue, $|0^-,000\rangle$: red, $|1^+,111\rangle$: black, $|1^+,110\rangle$: green, $|1^-,111\rangle$: orange, $|1^-,110\rangle$: magenta, sum of the six populations: blue dashed line) and coarse-grained populations in $J$ (upper right panel—$J$ = 0: blue, $J$ = 1: red, sum of the $J$ = 0 and $J$ = 1 coarse-grained populations: blue dashed) as a function of time $t$ for the tunneling enhancement scheme for $NHD_2$. The lower left and right panels show $p_{rev}(t) = |\langle\Psi(0)|\Psi(t)\rangle|^2$ and $P_R(t)$ (tunneling enhancement scheme: blue, field-free dynamics: red), respectively. The black dashed curves indicate the envelope function of the laser pulse [$f(t) = \sin^2(\pi t/t_p)$]. The parameters of the laser pulse are $\tilde{\nu}_0 = 825.0\,\mathrm{cm}^{-1}$, $I_{max}$ = 5.85 GW cm$^{-2}$, and $t_p$ = 25 ps.

The initial state is again chosen as the $(\Phi_{v^+}+\Phi_{v^-})/\sqrt{2}$ linear combination of the symmetric and antisymmetric tunneling eigenstates $\Phi_{v^+}$ and $\Phi_{v^-}$ of a selected tunneling doublet, giving rise to a simple periodic time evolution of the associated probability density [see Eq. (53)]. According to Eq. (50), one has to evaluate the step function matrix element $h(q) = \langle\Phi_{v^+}|\hat{h}|\Phi_{v^-}\rangle$, given as a function of the pyramid height $q$ for the $v$ = 0, $v$ = 1, and $v$ = 2 tunneling doublets, where $v$ specifies the number of vibrational quanta in the inversion mode and the remaining five vibrational quantum numbers are zero. The corresponding 6D tunneling splittings $\Delta E_{\pm,v}$ and tunneling periods $\tau_v$ evaluated with the AMMPOT4 PES are $\Delta E_{\pm,v=0}$ = 0.75 cm$^{-1}$, $\Delta E_{\pm,v=1}$ = 33.95 cm$^{-1}$ and $\Delta E_{\pm,v=2}$ = 277.53 cm$^{-1}$, and $\tau_{v=0}$ = 44.42 ps, $\tau_{v=1}$ = 0.98 ps, and $\tau_{v=2}$ = 0.12 ps, respectively. The $h(q)$ functions, obtained by full-dimensional GENIUSH computations, are compared (see Fig. 15) to the 1D results published by Manz and co-workers,[93] who used the 1D model potential of Ref. 152 and assumed $C_{3v}$ symmetry, constant NH bond lengths, and a constant effective tunneling mass along the inversion reaction path. Despite the approximate nature of the 1D results reported in Ref. 93, we have found excellent agreement between the 6D and 1D $h(q)$ functions, as shown

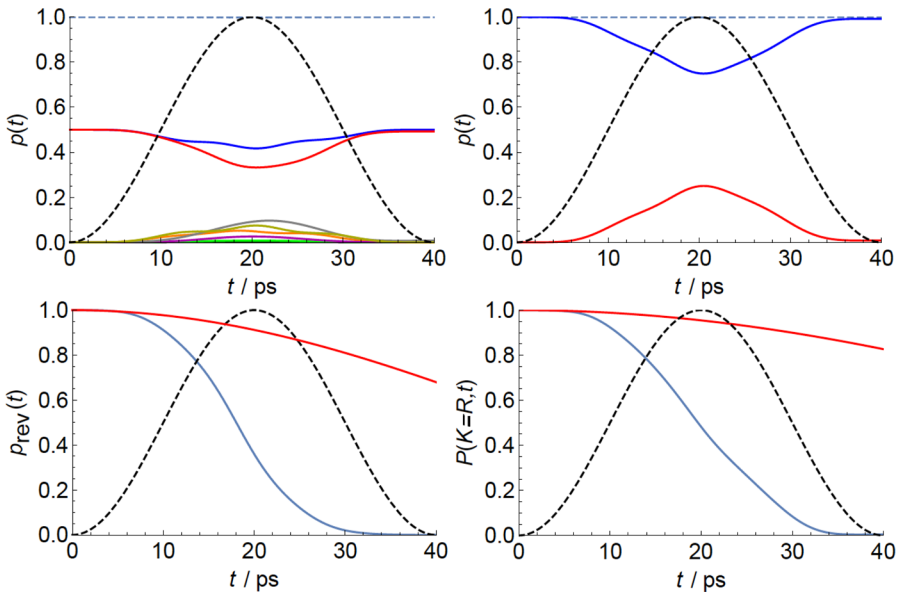


**FIG. 14**. Populations of selected eigenstates (upper left panel—$|0^+,000\rangle$: blue, $|0^-,000\rangle$: red, $|1^+,101\rangle$: black, $|1^+,111\rangle$: green, $|1^+,110\rangle$: orange, $|1^-,101\rangle$: magenta, $|1^-,111\rangle$: gray, $|1^-,110\rangle$: yellow, sum of the eight populations: blue dashed) and coarse-grained populations in $J$ (upper right panel—$J$ = 0: blue, $J$ = 1: red, sum of the $J$ = 0 and $J$ = 1 coarse-grained populations: blue dashed line) as a function of time $t$ for the tunneling enhancement scheme for NHDT. The lower left and right panels show $p_{rev}(t) = |\langle\Psi(0)|\Psi(t)\rangle|^2$ and $P(K = R, t)$ (tunneling enhancement scheme: blue, field-free dynamics: red), respectively. The black dashed curves indicate the envelope function of the laser pulse [$f(t) = \sin^2(\pi t/t_p)$]. The parameters of the laser pulse are $\tilde{\nu}_0 = 793.5\,\mathrm{cm}^{-1}$, $I_{max}$ = 3.15 GW cm$^{-2}$, and $t_p$ = 40 ps.

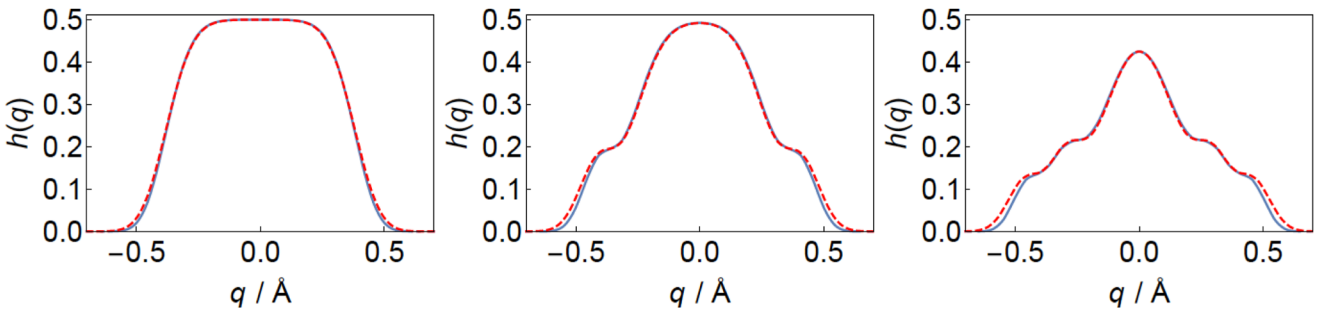


**FIG. 15**. Comparison of 6D (shown in blue) and 1D (shown in red) $h(q) = \left\langle \Phi_{v^+} \middle| \hat{h}(\mathbf{Q}; q) \middle| \Phi_{v^-} \right\rangle$ matrix elements (profile of the tunneling flux, see the text for explanation) as a function of $q$ (pyramid height in Å) for the tunneling doublets of $NH_3$ with $v = 0$ (left panel), $v = 1$ (middle panel), and $v = 2$ (right panel).

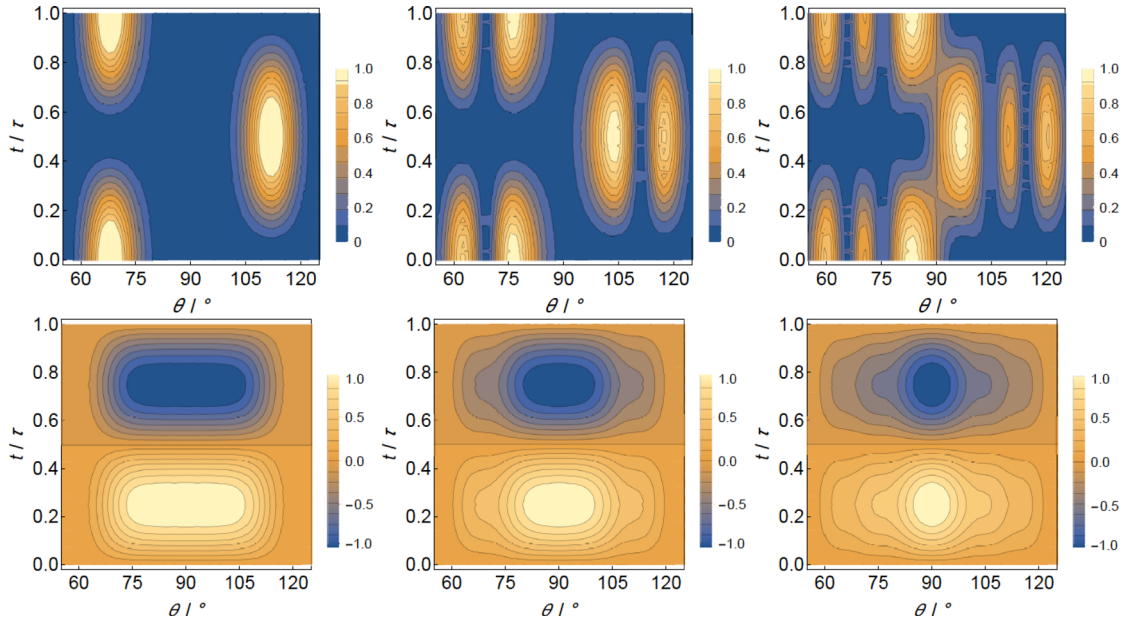


**FIG. 16**. Inversion probability densities (upper panels) and flux densities (lower panels) shown as a function of the inversion angle $\theta$ and time $t$ for the tunneling doublets of $NH_3$ with $v = 0$ (left panels, $\tau_{v=0} = 44.42$ ps), $v = 1$ (middle panels, $\tau_{v=1} = 0.98$ ps), and $v = 2$ (right panels, $\tau_{v=2} = 0.12$ ps), where $\tau_v$ is the tunneling period. Note that the data are normalized to the ranges [0, 1] (probability density) and [−1, 1] (flux density).

in Fig. 15. Besides the excellent numerical agreement, our results also confirm two interesting qualitative observations: (a) the nuclear-motion flux has its maximum at the potential barrier, as already inferred in Ref. 90; (b) the $h(q)$ functions show so-called staircase patterns, the shape of $h(q)$ for a given inversion quantum number $v$ can be described as a symmetric staircase with $v + 1$ steps up and down.[93] Figure 16 shows the time-dependent probability densities and flux densities as a function of $\theta$ for the initial state $(\Phi_{v^+} + \Phi_{v^-})/\sqrt{2}$ with $v = 0, 1, 2$, obtained again by 6D GENIUSH computations. The staircase structure of the nuclear flux densities is also apparent from Fig. 16, and comparing the probability densities to the corresponding flux densities reveals that the staircase patterns are caused by the lobe structures observed in the probability densities.[93]

## V. DISCUSSION AND CONCLUSIONS

As a prototypical molecule for spectroscopy and quantum dynamics, ammonia has been the subject of numerous investigations. The principal goal of our current work is to provide, for the first time, a full-dimensional quantum-dynamical treatment of the time-dependent rovibrational motion in the electronic ground state, including stereomutation by tunneling as well as for the isolated molecule under coherent infrared laser excitation. Thus, all relevant degrees of

freedom are included explicitly, except the nuclear spin degrees of freedom which are included implicitly by symmetry effects, but the dynamics of which are expected to occur on time scales much longer than those considered here. Similarly, excitation of the electronic degrees of freedom and ionization are not expected in the intensity and frequency ranges relevant here. The accuracy of the theoretical results is limited mainly by the uncertainties in the underlying PES and DMS. While these are not, strictly speaking, of spectroscopic accuracy, they represent nevertheless the available high-resolution spectroscopic data with sufficient accuracy that one can expect our results to provide a realistic description of the main quantum-dynamical phenomena presented here for several ammonia isotopomers, as they would be found in experiments under similar conditions in a time window between 0 and 500 ps, typically. This conclusion is supported by the comparison of results obtained with two current PES,[14,17] which give quite similar results for energies up to and beyond 1 eV as relevant for the present work.

Our investigation is enabled by several methodological developments reported here and in part in earlier work. Our further development within the program package GENIUSH, using a contracted vibrational subspace method,[76,105] has allowed the computation of rovibrational eigenstates and energies up to high excitations. We newly included the computational methods for solving the TDSE including coherent radiative excitation. To this end, the GENIUSH code[73–76] is extended to handle explicitly time-dependent operators. The TDSE is represented in the basis of molecular eigenstates and solved with a Chebyshev time propagator method,[34,35] including a Floquet approximation approach.[42,43] Thus, we are able to describe the time-dependent dynamics under conditions simulating laboratory experiments with coherent laser excitation.

An important motivation for theoretical studies of time-dependent molecular quantum dynamics arises from the long-standing goal of controlling chemical reactions by laser irradiation.[55–67,153] Control of molecular dynamics by coherent radiation can take several forms. In one approach, one aims at selective population transfer to individual quantum states, including simple superpositions, by suitably selected radiation pulses. This has been achieved early on in the radiofrequency and microwave domain,[148,154,155] but there have also been important later developments in the optical domain, including some very recent relevant applications.[29,72,135,156–158]

In a second approach, one uses vibrationally mode-selective short-pulse excitation to states which show mode-selective chemistry following the excitation. In the present context of tunneling stereomutation in ammonia isotopomers, the excitation would be directed towards vibrational levels where the tunneling stereomutation can be either enhanced or inhibited. One can qualitatively extract from the tunneling splittings exhibited by the eigenstate results for the excited vibrational levels whether enhancement or inhibition apply (see Tables I–III), although with intense coherent excitation further levels must be considered as well, as has been discussed for ammonia already on the basis of lower-dimensional computations.[77–79,82,83] The vibrationally mode-selective change of tunneling splittings can also be obtained from high-resolution spectroscopy,[22–27] the results of which compare favorably with our eigenstate computations. In this context, the role of intramolecular vibrational redistribution (IVR) is of interest. Indeed, mode-selective modifications of tunneling splittings can arise in a vibrationally adiabatic picture, which can be treated theoretically with the quasiadiabatic channel RPH approximation (without IVR).[10,11] Alternatively, explicit anharmonic intermode coupling with the tunneling mode by IVR can modify the tunneling splittings importantly. Our results in Sec. III have shown that for ammonia ($NHD_2$) the vibrationally adiabatic RPH approximation breaks down and the inclusion of anharmonic intermode coupling in the full-dimensional rovibrational approach is essential. This is very different from the stereomutation in the hydrogen peroxide isotopomers, where the quasiadiabatic channel RPH approximation works well, even quantitatively, for the tunneling process.[10,11]

A third approach towards the control of tunneling has been in the focus of the present study: one can modify the effective dynamics during excitation with well-designed laser pulses and control tunneling thereby. This amounts in essence to studying the molecular states dressed by the coherent field. Inhibition as well as enhancement of tunneling can be achieved this way. The inhibition strategy is related to the coherent destruction of tunneling proposed in Ref. 122, while the enhancement strategies use the adiabatic Floquet theory.[124,125] In contrast to the simple model systems studied before, we demonstrate these phenomena by a realistic full-dimensional treatment of the ammonia isotopomers $NHD_2$ and NHDT (Sec. IV). The Floquet formalism is applied here to a well-selected subset of six to eight rotational-vibrational eigenstates, where it is used to design specific laser fields that are able to demonstrate either the inhibition or the enhancement of tunneling. To test the thus designed laser pulses, accurate time-dependent computations in a high-dimensional set of rotation-vibration-tunneling eigenstates (about 16 000 in total) have been carried out. Tunneling can be coherently inhibited in $NHD_2$ by a continuous-wave laser with a carrier wavenumber of 810 $cm^{-1}$ and an intensity of 7.77 GW $cm^{-2}$. In NHDT, the corresponding parameters are 780 $cm^{-1}$ and 7.56 GW $cm^{-2}$ to observe similar phenomena. In the case of $NHD_2$, the carrier wavenumber is similar to the value from a "vibration-only model," where rotations are completely neglected and supposing that the molecule was oriented prior to the interaction with the laser field[83] (see also 4D computations in Ref. 77).

On the other hand, tunneling can be enhanced by an off-resonant laser pulse with a $\sin^2(\pi t/t_p)$ envelope function with duration $t_p$ = 25 ps in the case of $NHD_2$ and 40 ps for NHDT. The carrier wavenumbers are 825 $cm^{-1}$ ($NHD_2$) and 793.5 $cm^{-1}$ (NHDT). The corresponding maximum intensities are 5.85 GW $cm^{-2}$ and 3.15 GW $cm^{-2}$, respectively. The $J$ = 1 rotationally excited eigenstates (absent in vibration-only models such as

in Refs. 82 and 83) are essential transient states to achieve this enhancement scheme.

The verification of the laser-field design by full-dimensional quantum-dynamical computations is crucial. Applying the Floquet formalism to reduced sets of rotation-vibration-tunneling eigenstates is an efficient method to laser-field design. However, oversimplified models can lead to inaccurate laser-field designs, when they do not represent sufficiently well the quantum-dynamical results using the full set of eigenstates. In this case, the set of states used within the Floquet formalism has to be extended, as has been documented in the present work. Identifying eigenstates with approximate "good" quantum numbers has proved useful in this context.

The chiral isotopomer NHDT is of particular interest as it allows for a study of a true chemical reaction, the enantiomerisation by stereomutation tunneling. The time-dependent population for each enantiomer can be followed in full-dimensional quantum dynamics. Ammonia provides here an example complementary to the enantiomerisation of hydrogen peroxide, HOOH, as the role of IVR is very different in these two molecules. On the other hand, parity violation can be neglected similarly in both cases, as the tunneling splittings dominate over the parity violating potentials by many orders of magnitude.[110] This can be contrasted with molecules such as ClOOCl and ClSSCl, where theory predicts parity violation to dominate over tunneling.[135,159] Our developments for full-dimensional rovibrational dynamics also open the route towards future full-dimensional studies of chiral molecules including parity violating potentials, so far studied only with approximate theories using quasiadiabatic channel RPH treatments[135] or reduced-dimensional models.[160,161]

Further insight into the stereomutation dynamics was provided by our study of the flux function following Ref. 93, but here in a full-dimensional approach. Our results indicate that the 1D model is surprisingly accurate, as well as accounting for the flux maximum and also for demonstrating the staircase shape of the flux function $h(q)$ (Sec. IV D). For the sake of comparison with the 1D model, we have restricted these calculations to a full-dimensional vibrational calculation for $NH_3$ (omitting rotation). It must be noted, however, that in the real ammonia molecule $NH_3$, because of nuclear-spin symmetry, there is no ground-state tunneling doublet for $J = 0$, the lowest such doublet occurs for $J = 1$ (see, e.g., Refs. 29 and 162). This effect cannot be recovered by a pure vibrational model (neither 1D nor 6D), but it is, of course, included in our full-dimensional rotation-vibrational-tunneling calculations. Our work also paves the way for future extended full-dimensional studies of tunneling dynamics of ammonia isotopomers. These will include the analysis of the interplay of rotational and vibrational excitation in such tunneling systems under coherent excitation. One can investigate the possibilities for statistical mixing of modes in highly excited ammonia, of which we have seen here the first signatures due to the importance of IVR in $NHD_2$. Finally, at very long times and high density of states, the quantum dynamics should also include the possibilities of nuclear spin symmetry and even parity mixing as expected in general for polyatomic molecules in the limit of high densities of states.[149,163]

## SUPPLEMENTARY MATERIAL

See supplementary material for the complete list of rotational-vibrational energy levels used in this study.

## ACKNOWLEDGMENTS

This work was supported financially by the Swiss SNF, ETH Zürich (in particular, the Laboratory of Physical Chemistry), an ERC Advanced Grant No. 290925, the COST project MOLIM: Molecules in Motion (CM1405), and NKFIH (Grant Nos. PD124699 and K119658). This research was also supported by the European Union and the State of Hungary and co-financed by the European Regional Development Fund (Grant No. VEKOP-2.3.2-16-2017-00014). Sergey Yurchenko is gratefully acknowledged for useful discussions and providing the NH3-Y2010 potential energy and electric dipole moment subroutines. We thank Jörn Manz for fruitful discussions on nuclear-motion flux. We acknowledge the help and support from, as well as discussions with Tucker Carrington, Ziqiu Chen, Frédéric Merkt, Robert Prentner, Georg Seyfang, Jürgen Stohner, Ioannis Thanopulos, and Gunther Wichmann. C.F. is grateful to the COST Project No. CM1405, MOLIM: Molecules in Motion for funding a short-term scientific mission at ETH Zürich.

## REFERENCES

[1] F. Hund, Z. Phys. **43**, 805 (1927).
[2] G. Herzberg, *Molecular Spectra and Molecular Structure: Infrared and Raman Spectra of Polyatomic Molecules* (Van Nostrand, Reinhold, New York, 1945), Vol. 2.
[3] F. Merkt and M. Quack, "Molecular quantum mechanics and molecular spectra, molecular symmetry, and interaction of matter with radiation," in *Handbook of High-Resolution Spectroscopy*, edited by M. Quack and F. Merkt (John Wiley & Sons, Ltd., 2011), Vol. 1, pp. 1–55.
[4] A. G. Császár, C. Fábri, T. Szidarovszky, E. Mátyus, T. Furtenbacher, and G. Czakó, Phys. Chem. Chem. Phys. **14**, 1085 (2012).
[5] R. Marquardt and M. Quack, "Global analytical potential energy surfaces for high-resolution molecular spectroscopy and reaction dynamics," in *Handbook of High-Resolution Spectroscopy*, edited by M. Quack and F. Merkt (John Wiley & Sons, Ltd., 2011), Vol. 1, pp. 511–549.
[6] T. Carrington, "Using iterative methods to compute vibrational spectra," in *Handbook of High-Resolution Spectroscopy*, edited by M. Quack and F. Merkt (John Wiley & Sons, Ltd., 2011), Vol. 1, pp. 573–585.
[7] J. Tennyson, "High accuracy rotation-vibration calculations on small molecules," in *Handbook of High-Resolution Spectroscopy*, edited by M. Quack and F. Merkt (John Wiley & Sons, Ltd., 2011), Vol. 1, pp. 551–571.
[8] J. Breidung and W. Thiel, "Prediction of vibrational spectra from *ab initio* theory," in *Handbook of High-Resolution Spectroscopy*, edited by M. Quack and F. Merkt (John Wiley & Sons, Ltd., 2011), Vol. 1, pp. 389–403.
[9] Y. Yamaguchi and H. F. Schaefer III, "Analytic derivative methods in molecular electronic structure theory: A new dimension to quantum chemistry and its applications to spectroscopy," in *Handbook of High-Resolution Spectroscopy*, edited by M. Quack and F. Merkt (John Wiley & Sons, Ltd., 2011), Vol. 1, pp. 325–362.

[10]B. Fehrensen, D. Luckhaus, and M. Quack, Chem. Phys. **338**, 90 (2007).
[11]B. Fehrensen, D. Luckhaus, and M. Quack, Chem. Phys. Lett. **300**, 312 (1999).
[12]D. Luckhaus, J. Chem. Phys. **113**, 1329 (2000).
[13]R. Marquardt, K. Sagui, W. Klopper, and M. Quack, J. Phys. Chem. B **109**, 8439 (2005).
[14]R. Marquardt, K. Sagui, J. Zheng, W. Thiel, D. Luckhaus, S. Yurchenko, F. Mariotti, and M. Quack, J. Phys. Chem. A **117**, 7502 (2013).
[15]R. Marquardt, M. Quack, I. Thanopulos, and D. Luckhaus, J. Chem. Phys. **119**, 10724 (2003).
[16]S. N. Yurchenko, R. J. Barber, A. Yachmenev, W. Thiel, P. Jensen, and J. Tennyson, J. Phys. Chem. A **113**, 11845 (2009).
[17]S. N. Yurchenko, R. J. Barber, J. Tennyson, W. Thiel, and P. Jensen, J. Mol. Spectrosc. **268**, 123 (2011).
[18]P. A. Coles, R. I. Ovsyannikov, O. L. Polyansky, S. N. Yurchenko, and J. Tennyson, J. Quant. Spectrosc. Radiat. Transfer **219**, 199 (2018).
[19]S. N. Yurchenko, W. Thiel, and P. Jensen, J. Mol. Spectrosc. **245**, 126 (2007).
[20]A. Yachmenev and S. N. Yurchenko, J. Chem. Phys. **143**, 014105 (2015).
[21]S. N. Yurchenko, A. Yachmenev, and R. I. Ovsyannikov, J. Chem. Theory Comput. **13**, 4368 (2017).
[22]M. Snels, L. Fusina, H. Hollenstein, and M. Quack, Mol. Phys. **98**, 837 (2000).
[23]M. Snels, H. Hollenstein, and M. Quack, J. Chem. Phys. **119**, 7893 (2003).
[24]M. Snels, H. Hollenstein, and M. Quack, J. Mol. Spectrosc. **237**, 143 (2006).
[25]M. Snels, H. Hollenstein, and M. Quack, J. Chem. Phys. **125**, 194319 (2006).
[26]M. Snels, V. Horká-Zelenková, H. Hollenstein, and M. Quack, "High resolution FTIR and diode laser spectroscopy of supersonic jets," in *Handbook of High-Resolution Spectroscopy*, edited by M. Quack and F. Merkt (John Wiley & Sons, Ltd., 2011), Vol. 2, pp. 1021–1067.
[27]A. G. Császár and T. Furtenbacher, Phys. Chem. Chem. Phys. **18**, 1092 (2016).
[28]A. Yachmenev and J. Küpper, J. Chem. Phys. **147**, 141101 (2017).
[29]P. Dietiker, E. Miloglyadov, M. Quack, A. Schneider, and G. Seyfang, J. Chem. Phys. **143**, 244305 (2015).
[30]Z. Bačić and J. C. Light, Annu. Rev. Phys. Chem. **40**, 469 (1989).
[31]J. C. Light and T. Carrington, Adv. Chem. Phys. **114**, 263 (2000).
[32]R. Kosloff and D. Kosloff, J. Comput. Phys. **63**, 363 (1986).
[33]R. Kosloff, J. Phys. Chem. **92**, 2087 (1988).
[34]H. Tal-Ezer and R. Kosloff, J. Chem. Phys. **81**, 3967 (1984).
[35]U. Peskin, R. Kosloff, and N. Moiseyev, J. Chem. Phys. **100**, 8849 (1994).
[36]C. Leforestier, R. H. Bisseling, C. Cerjan, M. D. Feit, R. Friesner, A. Guldberg, A. Hammerich, G. Jolicard, W. Karrlein, H.-D. Meyer, N. Lipkin, O. Roncero, and R. Kosloff, J. Comput. Phys. **94**, 59 (1991).
[37]H.-D. Meyer, U. Manthe, and L. Cederbaum, Chem. Phys. Lett. **165**, 73 (1990).
[38]*Multidimensional Quantum Dynamics: MCTDH Theory and Applications*, edited by H.-D. Meyer, G. A. Worth, and F. Gatti (Wiley-VCH Verlag GmbH & Co. KGaA, 2009).
[39]M. H. Beck, A. Jäckle, G. A. Worth, and H.-D. Meyer, Phys. Rep. **324**, 1 (2000).
[40]R. Marquardt, ChemPhysChem **14**, 1350 (2013).
[41]E. Schrödinger, Naturwissenschaften **14**, 664 (1926).
[42]M. Quack, J. Chem. Phys. **69**, 1282 (1978).
[43]M. Quack, Adv. Chem. Phys. **50**, 395 (1982).
[44]M. Quack, Infrared Phys. **29**, 441 (1989).
[45]R. Marquardt and M. Quack, J. Chem. Phys. **90**, 6320 (1989).
[46]M. Quack and E. Sutcliffe, J. Chem. Phys. **83**, 3805 (1985).
[47]M. Quack, Infrared Phys. Technol. **36**, 365 (1995).
[48]M. Quack, "Time dependent intramolecular quantum dynamics from high resolution spectroscopy and laser chemistry," in *Time-Dependent Quantum Molecular Dynamics*, edited by J. Broeckhove and L. Lathouwers (Springer US, Boston, MA, 1992), pp. 293–310.
[49]G. Seyfang and M. Quack, Nachr. Chem. **66**, 307 (2018).
[50]J. P. Klinman and A. Kohen, Annu. Rev. Biochem. **82**, 471 (2013).
[51]P. R. Schreiner, H. P. Reisenauer, F. C. Pickard IV, A. C. Simmonett, W. D. Allen, E. Mátyus, and A. G. Császár, Nature **453**, 906 (2008).
[52]P. R. Schreiner, H. P. Reisenauer, D. Ley, D. Gerbig, C.-H. Wu, and W. D. Allen, Science **332**, 1300 (2011).
[53]T. Firmino, R. Marquardt, F. Gatti, and W. Dong, J. Phys. Chem. Lett. **5**, 4270 (2014).
[54]D. Zanuttini, F. Gatti, and R. Marquardt, Chem. Phys. **509**, 3 (2018).
[55]C. Brif, R. Chakrabarti, and H. Rabitz, New J. Phys. **12**, 075008 (2010).
[56]T. Baumert and G. Gerber, Isr. J. Chem. **34**, 103 (1994).
[57]T. Brixner and G. Gerber, ChemPhysChem **4**, 418 (2003).
[58]C. Horn, M. Wollenhaupt, M. Krug, T. Baumert, R. de Nalda, and L. Bañares, Phys. Rev. A **73**, 031401 (2006).
[59]R. N. Zare, Science **279**, 1875 (1998).
[60]P. Brumer and M. Shapiro, Chem. Phys. Lett. **126**, 541 (1986).
[61]M. Shapiro and P. Brumer, *Quantum Control of Molecular Processes* (Wiley-VCH Verlag GmbH & Co. KGaA, 2012).
[62]R. J. Gordon and S. A. Rice, Annu. Rev. Phys. Chem. **48**, 601 (1997).
[63]P. Král, I. Thanopulos, and M. Shapiro, Rev. Mod. Phys. **79**, 53 (2007).
[64]J. Martin and D. Braun, J. Phys. B **41**, 115502 (2008).
[65]J. M. Villas-Bôas, A. O. Govorov, and S. E. Ulloa, Phys. Rev. B **69**, 125342 (2004).
[66]L. G. Rego, L. F. Santos, and V. S. Batista, Annu. Rev. Phys. Chem. **60**, 293 (2009).
[67]V. Averbukh, S. Osovski, and N. Moiseyev, Phys. Rev. Lett. **89**, 253201 (2002).
[68]P. Ranitovic, C. W. Hogle, P. Rivière, A. Palacios, X.-M. Tong, N. Toshima, A. González-Castrillo, L. Martin, F. Martín, M. M. Murnane, and H. Kapteyn, Proc. Natl. Acad. Sci. U. S. A. **111**, 912 (2014).
[69]F. Krausz and M. Ivanov, Rev. Mod. Phys. **81**, 163 (2009).
[70]H. J. Wörner and P. B. Corkum, "Attosecond spectroscopy," in *Handbook of High-Resolution Spectroscopy*, edited by M. Quack and F. Merkt (John Wiley & Sons, Ltd., 2011), Vol. 3, pp. 1781–1804.
[71]L. Gallmann and U. Keller, "Femtosecond and attosecond light sources and techniques for spectroscopy," in *Handbook of High-Resolution Spectroscopy*, edited by M. Quack and F. Merkt (John Wiley & Sons, Ltd., 2011), Vol. 3, pp. 1805–1836.
[72]C. Fábri, S. Albert, Z. Chen, R. Prentner, and M. Quack, Phys. Chem. Chem. Phys. **20**, 7387 (2018).
[73]E. Mátyus, G. Czakó, and A. G. Császár, J. Chem. Phys. **130**, 134112 (2009).
[74]C. Fábri, E. Mátyus, and A. G. Császár, J. Chem. Phys. **134**, 074105 (2011).
[75]C. Fábri, E. Mátyus, and A. G. Császár, Spectrochim. Acta, Part A **119**, 84 (2014).
[76]C. Fábri, M. Quack, and A. G. Császár, J. Chem. Phys. **147**, 134101 (2017).
[77]R. Marquardt, M. Quack, I. Thanopulos, and D. Luckhaus, J. Chem. Phys. **118**, 643 (2003).
[78]R. Marquardt, M. Sanrey, F. Gatti, and F. Le Quéré, J. Chem. Phys. **133**, 174302 (2010).
[79]F. Gatti and R. Marquardt, Comput. Theor. Chem. **990**, 90 (2012).
[80]M. Schröder and A. Brown, J. Chem. Phys. **131**, 034101 (2009).
[81]K. Giri, E. Chapman, C. S. Sanz, and G. Worth, J. Chem. Phys. **135**, 044311 (2011).
[82]M. Sala, S. Guérin, F. Gatti, R. Marquardt, and H.-D. Meyer, J. Chem. Phys. **136**, 194308 (2012).
[83]M. Sala, F. Gatti, and S. Guérin, J. Chem. Phys. **141**, 164326 (2014).
[84]A. Owens, E. J. Zak, K. L. Chubb, S. N. Yurchenko, J. Tennyson, and A. Yachmenev, Sci. Rep. **7**, 45068 (2017).
[85]C. Fábri, R. Marquardt, and M. Quack, Chimia **68**, 531 (2014).
[86]C. Fábri, R. Marquardt, and M. Quack, in *Book of Abstracts of the XVIIth International Workshop on Quantum Atomic and Molecular Tunneling in Solids and Other Phases*, Beatenberg, Switzerland, 2015.

[87]C. Fábri, R. Marquardt, and M. Quack, in *Proceedings of the XXIst Symposium on Atomic, Cluster and Surface Physics 2018 (SASP 2018)* (Innsbruck University Press, Obergurgl, Austria, 2018), pp. 177–179.
[88]I. Barth, H.-C. Hege, H. Ikeda, A. Kenfack, M. Koppitz, J. Manz, F. Marquardt, and G. K. Paramonov, Chem. Phys. Lett. **481**, 118 (2009).
[89]T. Bredtmann, H. Katsuki, J. Manz, K. Ohmori, and C. Stemmle, Mol. Phys. **111**, 1691 (2013).
[90]J. Manz, A. Schild, B. Schmidt, and Y. Yang, Chem. Phys. **442**, 9 (2014).
[91]C. Liu, J. Manz, and Y. Yang, J. Phys. B: At., Mol. Opt. Phys. **48**, 164001 (2015).
[92]T. Bredtmann, D. J. Diestler, S.-D. Li, J. Manz, J. F. Pérez-Torres, W.-J. Tian, Y.-B. Wu, Y. Yang, and H.-J. Zhai, Phys. Chem. Chem. Phys. **17**, 29421 (2015).
[93]C. Liu, J. Manz, and Y. Yang, Phys. Chem. Chem. Phys. **18**, 5048 (2016).
[94]T. Bredtmann, J. Manz, and J.-M. Zhao, J. Phys. Chem. A **120**, 3142 (2016).
[95]G. Hermann, C. Liu, J. Manz, B. Paulus, J. F. Pérez-Torres, V. Pohl, and J. C. Tremblay, J. Phys. Chem. A **120**, 5360 (2016).
[96]D. Jia, J. Manz, B. Paulus, V. Pohl, J. C. Tremblay, and Y. Yang, Chem. Phys. **482**, 146 (2017).
[97]J. Manz, J. F. Pérez-Torres, and Y. Yang, Phys. Rev. Lett. **111**, 153004 (2013).
[98]M. Born and R. Oppenheimer, Ann. Phys. **389**, 457 (1927).
[99]M. Born and K. Huang, *Dynamical Theory of Crystal Lattices* (Clarendon Press, Oxford, 1954).
[100]S. Carter and N. Handy, Comput. Phys. Commun. **51**, 49 (1988).
[101]D. O. Harris, G. G. Engerholm, and W. D. Gwinn, J. Chem. Phys. **43**, 1515 (1965).
[102]M. J. Bramley and T. Carrington, Jr., J. Chem. Phys. **99**, 8519 (1993).
[103]F. T. Smith, Phys. Rev. Lett. **45**, 1157 (1980).
[104]H. Longuet-Higgins, Mol. Phys. **6**, 445 (1963).
[105]C. Fábri, E. Mátyus, T. Furtenbacher, L. Nemes, B. Mihály, T. Zoltáni, and A. G. Császár, J. Chem. Phys. **135**, 094307 (2011).
[106]R. Zare, *Angular Momentum: Understanding Spatial Aspects in Chemistry and Physics* (Wiley, New York, 1988).
[107]C. Eckart, Phys. Rev. **47**, 552 (1935).
[108]T. Szidarovszky, C. Fábri, and A. G. Császár, J. Chem. Phys. **136**, 174112 (2012).
[109]S. V. Krasnoshchekov, E. V. Isayeva, and N. F. Stepanov, J. Chem. Phys. **140**, 154104 (2014).
[110]M. Quack, "Fundamental symmetries and symmetry violations from high resolution spectroscopy," in *Handbook of High-Resolution Spectroscopy*, edited by M. Quack and F. Merkt (John Wiley & Sons, Ltd., 2011), Vol. 1, pp. 659–722.
[111]E. Mátyus, C. Fábri, T. Szidarovszky, G. Czakó, W. D. Allen, and A. G. Császár, J. Chem. Phys. **133**, 034113 (2010).
[112]J. Sarka, A. G. Császár, and E. Mátyus, Phys. Chem. Chem. Phys. **19**, 15335 (2017).
[113]D. Papp, T. Szidarovszky, and A. G. Császár, J. Chem. Phys. **147**, 094106 (2017).
[114]G. Floquet, Ann. Sci. Ec. Norm. Super. **12**, 47 (1883).
[115]M. Quack and J. Stohner, J. Phys. Chem. **97**, 12574 (1993).
[116]C. Cohen-Tannoudji, B. Diu, and F. Laloë, *Mécanique Quantique* (Hermann, 1973).
[117]S. Haroche, Ann. Phys. **14**, 189 (1971).
[118]S. Haroche, Ann. Phys. **14**, 327 (1971).
[119]J. H. Shirley, Phys. Rev. **138**, B979 (1965).
[120]H. P. Breuer, K. Dietz, and M. Holthaus, Z. Phys. D **8**, 349 (1988).
[121]E. P. Wigner, *Group Theory and Its Application to the Quantum Mechanics of Atomic Spectra* (Academic Press, New York, 1959).
[122]F. Grossmann, T. Dittrich, P. Jung, and P. Hänggi, Phys. Rev. Lett. **67**, 516 (1991).
[123]N. Sangouard, S. Guérin, M. Amniat-Talab, and H. R. Jauslin, Phys. Rev. Lett. **93**, 223602 (2004).
[124]M. Holthaus, Phys. Rev. Lett. **69**, 1596 (1992).
[125]S. Guérin and H. R. Jauslin, "Control of quantum dynamics by laser pulses: Adiabatic Floquet theory," in *Advances in Chemical Physics* (John Wiley & Sons, Inc., 2003), Vol. 125, pp. 147–267.
[126]S. Guérin and H. R. Jauslin, Phys. Rev. A **55**, 1262 (1997).
[127]E. Schrödinger, Ann. Phys. **386**, 109 (1926).
[128]W. H. Miller, J. Chem. Phys. **61**, 1823 (1974).
[129]W. H. Miller, S. D. Schwartz, and J. W. Tromp, J. Chem. Phys. **79**, 4889 (1983).
[130]W. H. Miller, Acc. Chem. Res. **26**, 174 (1993).
[131]W. H. Miller, J. Phys. Chem. A **102**, 793 (1998).
[132]U. Manthe, T. Seideman, and W. H. Miller, J. Chem. Phys. **101**, 4759 (1994).
[133]T. Wu, H.-J. Werner, and U. Manthe, Science **306**, 2227 (2004).
[134]M. Quack, Ber. Bunsenges. Phys. Chem. **88**, 94 (1984).
[135]R. Prentner, M. Quack, J. Stohner, and M. Willeke, J. Phys. Chem. A **119**, 12805 (2015).
[136]B. Fehrensen, D. Luckhaus, and M. Quack, Z. Phys. Chem. **209**, 1 (1999).
[137]L. Hofacker, Z. Naturforsch., A **18**, 607 (1963).
[138]M. Quack and J. Troe, Ber. Bunsenges. Phys. Chem. **78**, 240 (1974).
[139]W. H. Miller, N. C. Handy, and J. E. Adams, J. Chem. Phys. **72**, 99 (1980).
[140]E. R. Cohen, T. Cvitaš, J. G. Frey, B. Holmström, K. Kuchitsu, R. Marquardt, I. Mills, F. Pavese, M. Quack, J. Stohner, H. L. Strauss, M. Takami, and A. J. Thor, *Quantities, Units and Symbols in Physical Chemistry*, 3rd ed. (Royal Society of Chemistry, 2007).
[141]R. Berger, M. Quack, A. Sieben, and M. Willeke, Helv. Chim. Acta **86**, 4048 (2003).
[142]S. Hervé, F. Le Quéré, and R. Marquardt, J. Chem. Phys. **114**, 826 (2001).
[143]S. Hervé, F. Le Quéré, and R. Marquardt, J. Chem. Phys. **116**, 3300 (2002).
[144]M. Šindelka, N. Moiseyev, and L. S. Cederbaum, J. Phys. B: At., Mol. Opt. Phys. **44**, 045603 (2011).
[145]G. J. Halász, A. Vibók, M. Šindelka, N. Moiseyev, and L. S. Cederbaum, J. Phys. B: At., Mol. Opt. Phys. **44**, 175102 (2011).
[146]G. J. Halász, M. Šindelka, N. Moiseyev, L. S. Cederbaum, and A. Vibók, J. Phys. Chem. A **116**, 2636 (2012).
[147]T. Szidarovszky, G. J. Halász, A. G. Császár, L. S. Cederbaum, and A. Vibók, J. Phys. Chem. Lett. **9**, 2739 (2018).
[148]S. Kukolich, J. Wang, and D. Oates, Chem. Phys. Lett. **20**, 519 (1973).
[149]M. Quack, Angew. Chem., Int. Ed. **28**, 571 (1989).
[150]S. Albert, K. K. Albert, H. Hollenstein, C. M. Tanner, and M. Quack, "Fundamentals of rotation-vibration spectra," in *Handbook of High-Resolution Spectroscopy*, edited by M. Quack and F. Merkt (John Wiley & Sons, Ltd., 2011), Vol. 1, pp. 117–173.
[151]M. Quack, Mol. Phys. **34**, 477 (1977).
[152]J. R. Letelier and C. A. Utreras-Díaz, Spectrochim. Acta, Part A **53**, 247 (1997).
[153]D. W. Lupo and M. Quack, Chem. Rev. **87**, 181 (1987).
[154]R. R. Ernst, G. Bodenhausen, and A. Wokaun, *Principles of Nuclear Magnetic Resonance in One and Two Dimensions* (University Press, Oxford, 1987).
[155]A. Schweiger and G. Jeschke, *Principles of Pulse Electron Paramagnetic Resonance* (University Press, Oxford, 2001).
[156]K. Bergmann, H. Theuer, and B. W. Shore, Rev. Mod. Phys. **70**, 1003 (1998).
[157]N. V. Vitanov, A. A. Rangelov, B. W. Shore, and K. Bergmann, Rev. Mod. Phys. **89**, 015006 (2017).
[158]W. Dong, N. Mukherjee, and R. N. Zare, J. Chem. Phys. **139**, 074204 (2013).
[159]R. Berger, M. Gottselig, M. Quack, and M. Willeke, Angew. Chem., Int. Ed. **40**, 4195 (2001).
[160]M. Quack and J. Stohner, J. Chem. Phys. **119**, 11228 (2003).
[161]A. Bakasov, R. Berger, T.-K. Ha, and M. Quack, Int. J. Quantum Chem. **99**, 393 (2004).
[162]A. R. Al Derzi, T. Furtenbacher, J. Tennyson, S. N. Yurchenko, and A. G. Császár, J. Quant. Spectrosc. Radiat. Transf. **161**, 117 (2015).
[163]M. Quack, J. Chem. Phys. **82**, 3277 (1985).